IOPscience iopscience.iop.org

Home Search Collections Journals About Contact us My IOPscience

Predictive analysis of *q*-profile influence on transport in JET and ASDEX Upgrade hybrid scenarios

This article has been downloaded from IOPscience. Please scroll down to see the full text article.

2012 Plasma Phys. Control. Fusion 54 065008

(http://iopscience.iop.org/0741-3335/54/6/065008)

View the table of contents for this issue, or go to the journal homepage for more

Download details:
IP Address: 193.170.84.33
The article was downloaded on 24/05/2012 at 08:22

Please note that terms and conditions apply.

Plasma Phys. Control. Fusion **54** (2012) 065008 (19pp) doi:10.1088/0741-3335/54/6/065008

Predictive analysis of q-profile influence on transport in JET and ASDEX Upgrade hybrid scenarios

J Citrin[1], J Hobirk[2], M Schneider[3], J F Artaud[3], C Bourdelle[3], K Crombe[4], G M D Hogeweij[1], F Imbeaux[3], E Joffrin[3], F Koechl[5], J Stober[2], the ASDEX Upgrade team, JET-EFDA contributors[6] and the ITM-TF ITER Scenario Modelling group

JET-EFDA, Culham Science Centre, Abingdon, OX14 3DB, UK
[1] FOM Institute DIFFER-Dutch Institute for Fundamental Energy Research, Association EURATOM-FOM, Nieuwegein, The Netherlands
[2] MPI für Plasmaphysik, EURATOM Assoc., Boltzmannstr. 2, 85748 Garching, Germany
[3] CEA, IRFM, F-13108 Saint Paul Lez Durance, France
[4] Department of Applied Physics, Ghent University, Rozier 44, 9000 Ghent, Belgium
[5] Association EURATOM-ÖAW/ATI, Atominstitut, TU Wien, 1020 Vienna, Austria

E-mail: J.Citrin@differ.nl

Received 6 December 2011, in final form 4 April 2012
Published 23 May 2012
Online at stacks.iop.org/PPCF/54/065008

Abstract
Hybrid scenarios in present machines are often characterized by improved confinement compared with the IPB98(y,2) empirical scaling law expectations. This work concentrates on isolating the impact of increased s/q at outer radii (where s is the magnetic shear) on core confinement in low-triangularity JET and ASDEX Upgrade (AUG) experiments. This is carried out by predictive heat and particle transport modelling using the integrated modelling code CRONOS coupled to the GLF23 turbulent transport model. For both machines, discharge pairs were analysed displaying similar pedestal confinement yet significant differences in core confinement. From these comparisons, it is found that s/q shaping at outer radii may be responsible for up to ~50% of the relative core confinement improvement observed in these specific discharges. This relative improvement is independent of the degree of rotational shear turbulence suppression assumed in the GLF23 model. However, employing the full GLF23 rotational shear model leads to an overprediction of the ion temperatures in all discharges analysed. Additional mechanisms for core confinement improvement are discussed and estimated. Further linear threshold analysis with QuaLiKiz is carried out on both pairs of discharges. This work aims to validate recent predictions of the ITER hybrid scenario also employing CRONOS/GLF23, where a high level of confinement and resultant fusion power sensitivity to the s/q profile was found.

(Some figures may appear in colour only in the online journal)

1. Introduction

Over the past decade, an attractive operating scenario for the ITER tokamak has emerged, combining long discharge times similar to the steady-state scenario, while maintaining the reliability of the reference H-mode scenario. This so-called 'hybrid' scenario aims to maximize neutron fluence per shot by achieving an extended burn time ($t > 1000$ s in ITER) together with significant α-particle heating ($Q > 5$) [1]. The extended burn time is achieved by operation at reduced current and at a higher non-inductive current fraction compared

[6] See the appendix of F Romanelli *et al* 2010 *Proc. 23rd IAEA Fusion Energy Conf. (Daejeon, Korea).*

 © 2012 IOP Publishing Ltd Printed in the UK & the USA

with the reference H-mode scenario. The basis for this scenario has been established at DIII-D [2], AUG ('improved H-modes') [3], JET [4], JT-60 [5] and NSTX [6].

In present tokamaks, the hybrid scenario is characterized by a q-profile tailored to form a broad region of low magnetic shear, with q_0 typically close to unity. Operation at a β_N higher than in standard H-mode discharges is allowed by either a total avoidance of deleterious NTM triggering sawteeth ($q > 1$ everywhere) or by having sawteeth small or frequent enough such that the β_N limit for NTM triggering is significantly raised compared with standard H-mode discharges. These discharges frequently display improved confinement compared with the IPB98(y,2) empirical scaling law expectations, with H_{98} in the range 1–1.5. $H_{98} \equiv \tau_{th}/\tau_{IPB98(y,2)}$, where τ_{th} is the thermal confinement time and $\tau_{IPB98(y,2)}$ the empirical scaling law confinement time introduced in [7]. Assuming the same H_{98} factor as in present experiments, this performance extrapolates favourably in ITER, beyond the minimum $Q = 5$ ITER hybrid scenario requirement [8–10]. It is clearly of great importance to understand the source of improved confinement in present machines, to reliably extrapolate the scenario to ITER.

A number of possibilities explaining the confinement improvement have been proposed. One possibility is that the confinement dependence on β is not as strong as suggested by the IPB98(y,2) $\beta^{-0.9}$ scaling. The IPB98(y,2) scaling law was developed with discharges primarily in the range $\beta_N = 1$–2, lower than most hybrid discharges. Thus, if the β dependence would be in reality weaker, then the high β_N hybrid scenarios would display significantly higher confinement than expected from the IPB98(y,2) scaling. Indeed, a weaker β scaling than IPB98(y,2) has been found in dedicated experiments in DIII-D and JET [11, 12]. Furthermore, pedestal confinement improvement due to an increase in pedestal width with β_N is reported in AUG improved H-modes [13, 14]. However, in more recent experiments at JET, the β_N confinement scaling has been observed to depend on triangularity [15]. Low triangularity discharges display a weak β_N dependence, while high triangularity discharges display a strong edge confinement degradation with β_N in accordance with the IPB98(y,2) scaling.

Improved core confinement is seen in DIII-D hybrids and 'late-heating' AUG improved H-mode discharges, with electromagnetic gyrokinetic calculations showing that β-stabilization may be responsible for the core confinement improvement [14]. Rotation is seen to play an important role in improved confinement. Variable torque experiments at DIII-D by simultaneous application of co- and counter-beams led to a decrease in H_{98} from 1.5 to 1.1 in the extreme low rotation case (central $M \approx 0.15$) [16]. However, this H_{98} factor is still as high as in high rotation conventional H-mode plasmas. This shows that further factors are also responsible for core confinement improvement in hybrid scenarios, since the hybrid scenario at low rotation should exhibit a higher H_{98} factor than standard H-mode scenarios at low rotation. The precise mechanism of rotational shear core confinement improvement is also currently under investigation. Observations at JET point to the combination of low magnetic shear and high rotational shear leading to significantly reduced ion temperature profile stiffness [17, 18]. This is in opposition to the instability threshold offset observed in non-linear simulations and reproduced in reduced models such as GLF23 [19], which describe well the effect of rotation particularly for DIII-D [16]. Finally, the characteristic hybrid scenario q-profile shape—a central broad region of low magnetic shear, and increased magnetic shear towards the edge—may further contribute to improved confinement through a relative increase in s/q at outer radii, leading to an increase in the ITG threshold. This can be seen from the ITG threshold linear gyrokinetic analytical expression, in the flat density limit [20]:

$$\left(R/L_{T_i}\right)_{crit} = \frac{4}{3}(1 + T_i/T_e)\left(1 + 2\frac{s}{q}\right), \quad \text{with } R/L_n < 2(1 + T_i/T_e). \tag{1}$$

A similar dependence in the collisionless, flat density limit with both passing and trapped electrons was reported in modelling carried out with the Kinezero linear gyrokinetic code [21]. For $s > 0$ and for $T_i/T_e = 1$, the best fit of R/L_{T_i} following parameter scans in s and q was found as [22]

$$\left(R/L_{T_i}\right)_{crit} = 2\left(1.1 + 1.4\,s + 1.9\frac{s}{q}\right). \tag{2}$$

Similar s/q dependence has also been observed in electron heat transport experiments on Tore Supra [23, 24].

This work concentrates on isolating the impact of varying s/q at outer radii on core confinement in *low-triangularity* JET and AUG hybrid scenario experiments. For each machine, a pair of shots has been chosen which display a similar level of pedestal confinement yet a significant difference in core confinement. For each pair, the improved confinement case is correlated with a higher average s/q parameter. The aim of this work is to assess whether the predicted threshold improvement due to q-profile shaping is consistent with the observations. This is carried out by predictive heat and particle transport modelling using the integrated modelling code CRONOS [25] coupled to the GLF23 turbulent transport model [19, 26]. Successful validation of the GLF23 q-profile scaling has been carried out on DIII-D discharges at fixed magnetic shear [27]. The GLF23 modelling is supplemented by linear instability threshold calculations with the linear gyrokinetic code QuaLiKiz [28], based on the Kinezero code. One of the driving motivations of this work is to validate recent predictions of the ITER hybrid scenario also employing CRONOS/GLF23, where a high level of fusion power sensitivity to the s/q profile was found, even for relatively modest improvements in H_{98} [29].

This paper is organized as follows: the experimental discharges are described in section 2, the modelling tools and techniques in section 3, the GLF23 modelling results in section 4, additional mechanisms for core confinement improvement are discussed in section 5, the QuaLiKiz results in section 6, and the discussion and conclusions in section 7.

2. Experimental discharges

For both machines, discharge pairs were analysed displaying similar pedestal confinement yet significant differences in core

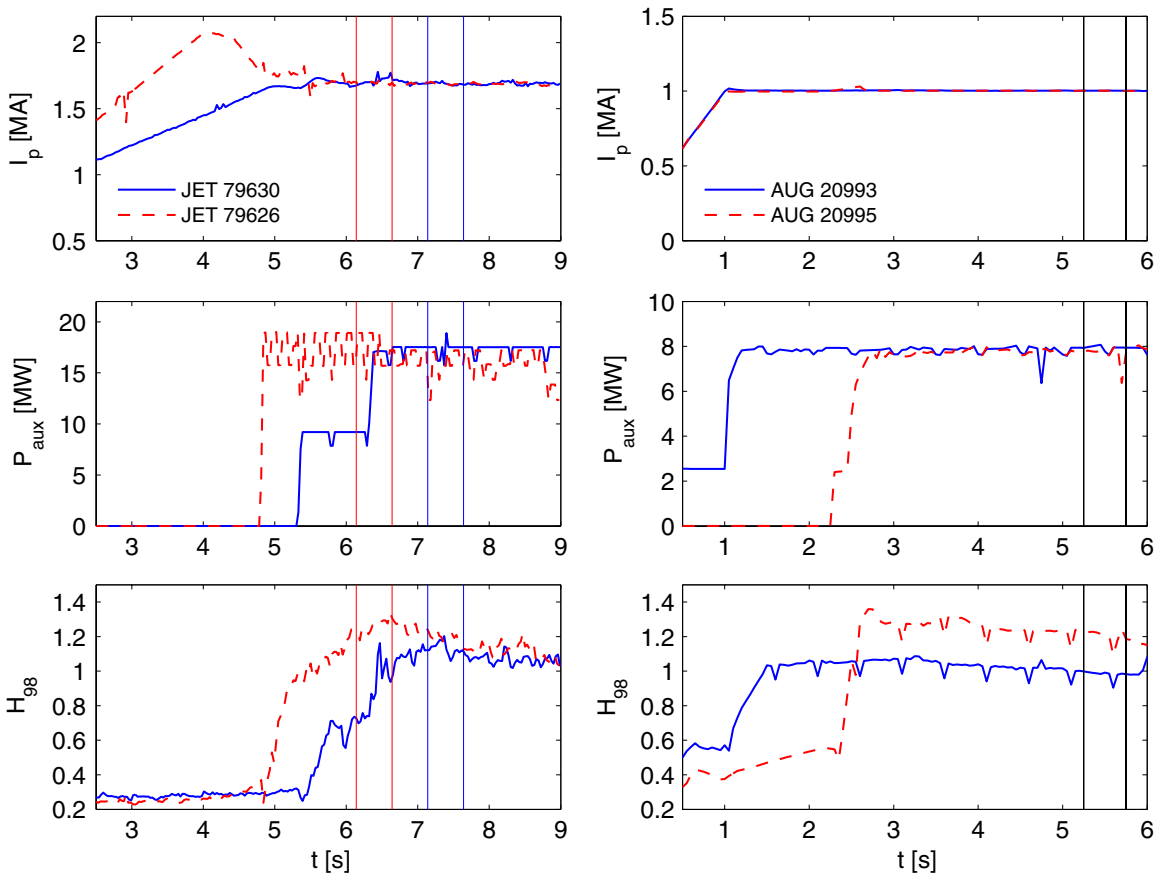

Figure 1. Temporal evolution of total plasma current (upper row), total auxilliary heating power $P_{aux} = P_{NBI} + P_{ICRH}$ (centre row) and H_{98} confinement factor (lower row) for the JET pair 79626/79630 (left panels) and AUG pair 20993/20995 (right panels).

confinement. A variation in q-profile was experimentally achieved in each pair. For the JET pair (79626/79630), this variation was achieved via the 'current-overshoot' method [10, 30]. With this method, the current is ramped down to its flattop value just prior to the main heating phase, resulting in a broader q-profile compared with a regular ramp-up scenario. For the AUG pair (20993/20995), the q-profile variation was achieved by varying the auxiliary heating timing, with the later heating case resulting in a broader q-profile [31]. Apart from the above-mentioned variations, all other control parameters (e.g. shaping, fueling, total heating power, PINI configuration) are kept the same between the discharges of each pair. The total flattop P_{aux} for the JET case is ≈17 MW, all from NBI. For the ASDEX case, flattop $P_{aux} \approx 8$ MW, with 5 MW from NBI and 3 MW from ICRH to reduce central tungsten impurity concentration. Temporal evolution of the total plasma current, heating power and confinement factor H_{98} for each pair can be seen in figure 1.

The vertical lines in the plots enclose the periods during which the kinetic profiles are averaged for analysis: 6.14–6.64 s for JET 79626, 7.14–7.64 s for JET 79630 and 5.25–5.75 s for both ASDEX discharges. The periods differ for JET due to the different heating scheme timings. Furthermore, it is during these periods that the pedestal confinement is similar for the two discharges. Following this period, the pedestal confinement in 79626 decays in time, contributing significantly to the observed reduction in H_{98} on a timescale significantly shorter than the current diffusion timescale. This behaviour is not a regular feature of JET hybrids with current overshoot at either low or high triangularity. For example, figure 1 in [10] illustrates improved confinement maintained throughout the flattop phase of a JET hybrid scenario discharge. We reiterate that the main purpose of this work is to isolate and validate the expected s/q impact on core confinement by comparing discharges in periods where they display similar pedestal confinement yet observed differences in both q-profile and core confinement. This is what is achieved by comparing the averaged kinetic profiles of the discharges within the above-mentioned time windows.

The degree of similarity of the pedestal confinement can be assessed by comparing the thermal β_N at the location of the GLF23 boundary conditions: $x = 0.83$ for the JET pair and 0.76 for the AUG pair. The values are 0.99/0.94 for JET 79626/79630, and 1.11/0.98 for AUG 20995/20993. The impact that these differences have on the core confinement is discussed in section 5.4, where core profile stiffness is assumed. Note that while the boundary condition values are related to the height of the edge transport barrier (pedestal), the correlation is not direct since the boundary condition locations for the GLF23 modelling do not coincide with the pedestal top. Particularly for the AUG simulations, the boundary condition is limited by the outermost data point of the T_i diagnostic, and no data on the actual T_i pedestal height is available. In principle, there may be differences in core confinement between the

Table 1. 0D quantities for all discharges analysed in this paper. Quantities are averaged over 7.14–7.64 s and 6.14–6.64 s for JET 79630 and 79626, respectively, and 5.25–5.75 s for AUG 20993 and 20995.

Shot	B_T (T)	I_p (MA)	β_N (W_{th})	β_N (W_{dia}/W_{mhd})	$\langle s/q \rangle$	Z_{eff}	H_{98}	MHD activity
JET 79630	2	1.7	1.9	2.6	0.79	1.97	1.13	Fishbones
JET 79626	2	1.7	2.1	2.8	0.94	1.76	1.26	Fishbones
AUG 20993	2.4	1	1.4	1.9	0.69	2.42	0.98	Weak 3/2 NTM
AUG 20995	2.4	1	1.7	2.3	0.84	2.35	1.2	Fishbones

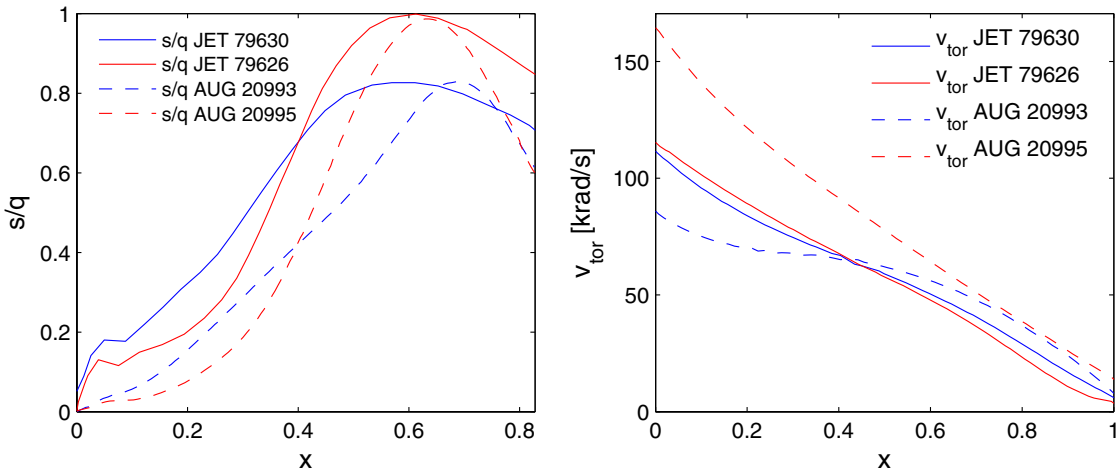

Figure 2. s/q profiles (left panel) and toroidal rotation profiles (right panel) for all discharges analysed in this paper.

actual pedestal top and the boundary condition taken for the GLF23 modelling. Thus we cannot relate with full certainty the differences in the GLF23 boundary condition values to differences in pedestal confinement.

All GLF23 analyses in this paper take background kinetic profiles and boundary conditions from the averaged periods defined above. Details of 0D quantities averaged over these periods can be found in table 1. $\langle s/q \rangle$ is defined as the volume averaged s/q between $x = 0.4$–0.8, where x is the normalized toroidal flux coordinate. The average is carried out from $x = 0.4$, since for $x < 0.4$ the magnetic shear is low ($s < 0.6$) and the short wavelength approximation within which equation (1) is derived may no longer hold. The averaging procedure is up to $x = 0.8$, the approximate location of the GLF23 boundary conditions. All discharges have fishbone activity, and are devoid of NTMs in the temporal periods studied, apart from AUG 20993, which has a 3/2 NTM in the vicinity of $x = 0.5$. The potential polluting effect of this mode on the isolation of the s/q impact on confinement for the AUG pair is examined in section 5.

The s/q and rotation profiles used throughout this analysis can be seen in figure 2, and the q-profiles themselves in figure 3. For each pair of discharges, the interpretative q-profiles are compared with the measured q-profiles obtained by MSE constrained equilibrium reconstruction. By interpretative q-profiles, we mean q-profiles predicted by CRONOS through solving the current diffusion equation with prescribed temperatures and densities (from measurement), and calculated current drive sources. For the JET case, the experimental and interpretative q-profiles agree to within 10% for $x \gtrsim 0.35$. For $x \lesssim 0.35$ the interpretative q-profiles have significantly lower values than the measured q-profiles. This discrepancy is limited to a region comprising only ~10% of the plasma volume, and thus plays a minor role in the determination of total core confinement, which is the central point of this work. It was thus decided to use the interpretative JET q-profiles for the GLF23 transport modelling in this work, since it was deemed that the current diffusion model could capture with higher fidelity than the measurements the subtle effect of current overshoot on the q-profile. The discrepancy for $x \lesssim 0.35$ may be due to MHD activity redistributing the current, clamping the q-profile to 1, as reported in [32–35]. The discrepancy within $x = 0.35$ is consistent with the lack of observed sawteeth in the JET pair. However, in principle $q < 1$ is a necessary but not sufficient condition for sawteeth. The sawtooth trigger can also depend on the magnetic shear at the inversion radius, the location of the inversion radius and the fast ion distribution function. Thus it is possible that no sawteeth are present in spite of $q < 1$ for these specific discharges. All JET interpretative simulations started at 2 s—early enough in the ramp-up phase such that the sensitivity of the q-profiles at the time of interest for the predictive simulations to the initial prescribed q-profiles is negligible. The initial prescribed q-profiles corresponded to a quadratic current profile constrained to satisfy l_i from EFIT reconstruction.

In the AUG pair, the interpretative q-profiles significantly departs from the measured q-profiles within a much greater bulk of the plasma volume compared with the JET pair. Such discrepancies between interpretative and measured q-profiles was also seen in previous AUG improved H-mode modelling [36]. This increased discrepancy may be due to

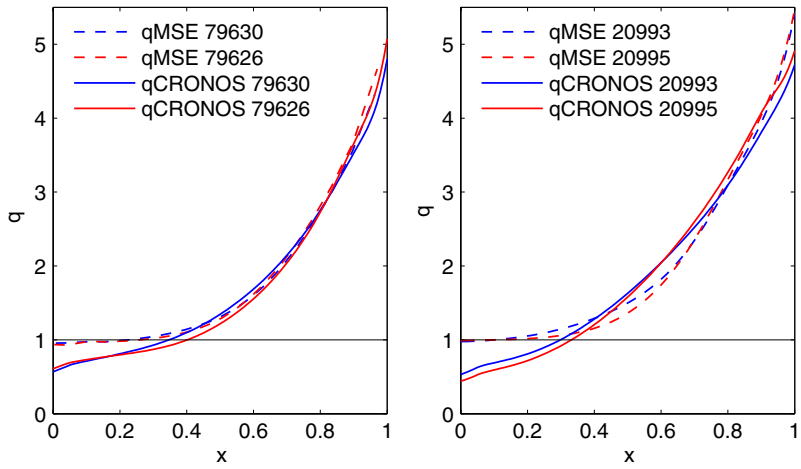

Figure 3. Comparison of interpretative and experimental q-profiles for the JET discharges (left panel) and for the AUG discharges (right panel).

a higher degree of current redistributed by MHD activity. It was thus decided to use the measured q-profiles for the GLF23 modelling for the AUG cases, since it is possible that neoclassical diffusion cannot account for the precise q-profile shape in the AUG case even at higher radii.

Regarding q-profile measurement errors, the MSE measurement error for the AUG q-profiles is $\sim$10%. For the JET q-profiles, the modelled values are sensitive to the measured $\langle Z_{\rm eff}\rangle$, $Z_{\rm eff}$ profile shape, and bootstrap current calculations. A thorough assessment of the q-profile sensitivity to the modelling assumptions has not been carried out for this work, apart from a $Z_{\rm eff}$ sensitivity check shown in section 4. However, both for the AUG and JET cases, the proximity of the shots (each pair was carried out in the same experimental session) means that it is likely that any systematic errors are the same for both discharges in each pair. Since we are concerned with *differences* in the q-profiles, this increases the reliability of the results. Nevertheless, it is indeed possible that the error in the difference between the q-profiles in each pair is of the order of the difference itself. This important caveat underlines this entire work.

The rotation profiles for the JET case are similar. For the AUG case, the 20993 (lower confinement) case has a significantly flatter rotation profile in the low magnetic shear region $x < 0.4$. It is possible that this flatter rotation profile is due to the magnetic braking induced by the 3/2 mode present in shot 20993.

A representative overview of the kinetic profile data and fit quality for all discharges analysed in this paper can be seen in figure 4 *for single timeslices*. Spline fits were carried out for each timeslice. The fit order (typically cubic or quartic) and break-points (typically near the pedestal if at all) varied between the different profiles. Note that the standard $\frac{\rm d}{{\rm d}x}|_{x=0}$ constraint on the profiles was not applied by the fitting routine used for this work. This constraint does not fundamentally change the profile shape in the region of interest for comparison with the GLF23 modelling ($x \sim$ 0.3–0.8). JET $T_{\rm i}$ was measured by a combination of core and edge charge-exchange (CXFM and CXSE) diagnostics. The CXSE is vital for determining the approximate equivalence of the $T_{\rm i}$ pedestal top values between the pair. However, the finite radial extension of the diagnostic does not allow the full resolution of the pedestal $T_{\rm i}$ profile. JET $T_{\rm e}$ was measured by both ECE and high resolution Thomson scattering (HRTS). The spline fit used both datasets on an equal footing. This is not ideal since the datasets are not fully mutually consistent. However, since the pedestal region (which will serve as the modelling boundary condition) is only resolved by HRTS, the choice of carrying out a combined data fit has no impact on the modelling results. Nevertheless, the lack of full agreement between the HRTS and ECE measurements should be maintained as a caveat when comparing the $T_{\rm e}$ modelling results with the fits from the experimental data. JET $n_{\rm e}$ was measured by HRTS.

For AUG, $T_{\rm i}$ was measured by CX. $T_{\rm e}$ was measured by ECE. $n_{\rm e}$ was measured by a combination of interferometry and lithium beam spectroscopy, and the data combined with the integrated data analysis (IDA) approach [37].

For comparison of the kinetic profiles with the GLF23 predictions, the profiles were averaged for 0.5 s during the time windows displayed in figure 1. This is more than an energy confinement time for both machines. This averaging also significantly reduces the RMS error of the data points, to below 2% for example for both the JET and AUG $T_{\rm i}$ and $V_{\rm tor}$ measurements. The boundary conditions for the GLF23 simulations were also taken from this averaging. From this averaging we can also analyse $R/L_{T_{\rm i}}$, to determine the location and robustness of the $R/L_{T_{\rm i}}$ differences between the shots of each pair. This can be seen in figure 5. These curves were made by time averaging the $T_{\rm i}$ spline fits made at each timeslice. $R/L_{T_{\rm i}}$ is calculated with respect to the average flux surface minor radius on the midplane, $r = (R_{\rm out} - R_{\rm in})/2$. The error from the scatter in these fits is 10% for the JET data, and 15% for the AUG data. We can see that the JET $R/L_{T_{\rm i}}$ differences are localized to the region $x =$ 0.6–0.8, while the AUG $R/L_{T_{\rm i}}$ differences are localized from $x =$ 0.25–0.7 (where $x = 0.25$ is the approximate location of the innermost reliable $T_{\rm i}$ datapoint). While the error bars lead to overlap over much of the $R/L_{T_{\rm i}}$ profiles, the errors are not independent. The scattering of one specific data point creates an opposing change in $R/L_{T_{\rm i}}$ on either side of the position of that point. This fact

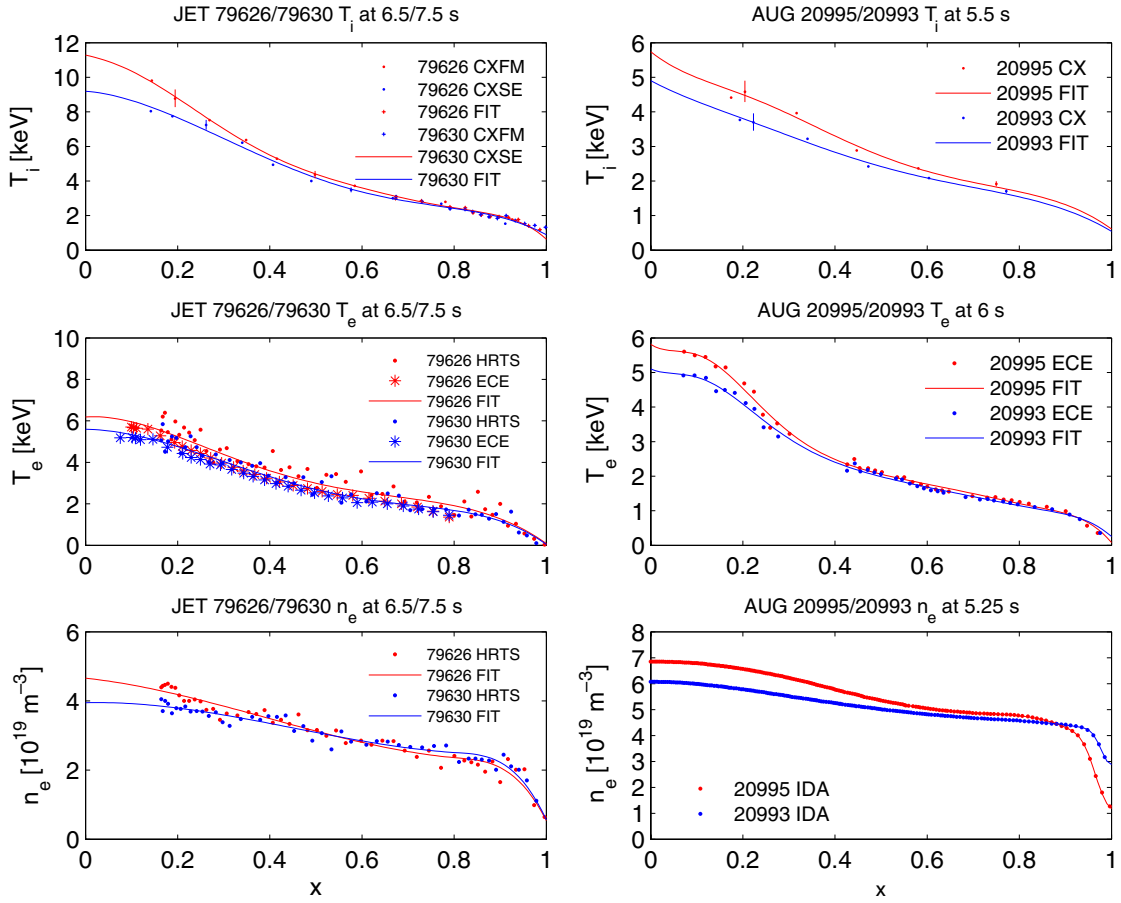

Figure 4. T_i (top row), T_e (centre row) and n_e (bottom row) profiles for JET 79626/30 (left panels) and AUG 20993/95 (right panels).

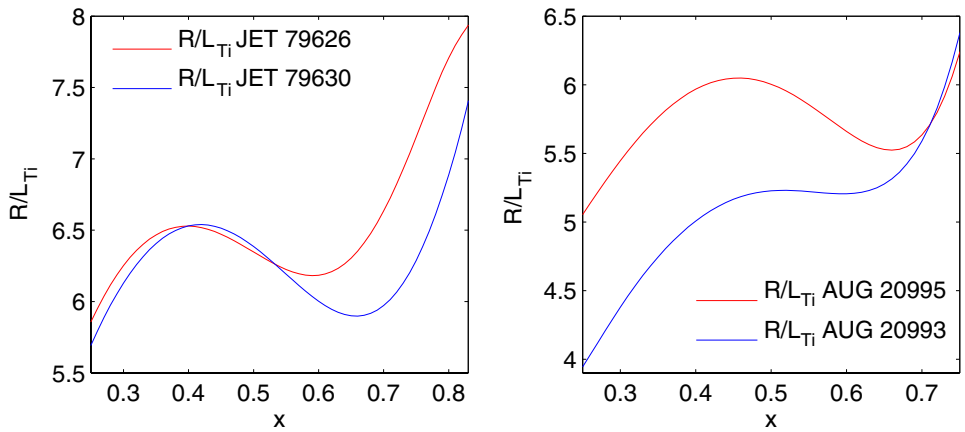

Figure 5. R/L_{T_i} profiles for JET 79626/30 (left panel) and AUG 20993/95 (right panel), for T_i profiles averaged over 0.5 s.

increases the robustness of the observed R/L_{T_i} differences and locations.

Finally, we compare the ratios of these experimental R/L_{T_i} profiles with the predicted analytical R/L_{T_i} ratios from equation (1), displayed in figure 6. We note that the R/L_n ratios of all discharges are low enough to satisfy the flat density profile approximation—$R/L_n < 2(1 + T_\mathrm{i}/T_\mathrm{e})$. This can be seen in figure 7, where the R/L_n values of the JET discharges (calculated with respect to $r = R_\mathrm{out} - R_\mathrm{in}$) are compared with $2(1 + T_\mathrm{i}/T_\mathrm{e})$. The constraint is satisfied to an even higher degree in the ASDEX pair, since the collisionality is higher and thus the density peaking reduced. In figure 6 we also include analytical R/L_{T_i} ratios also assuming constant $T_\mathrm{i}/T_\mathrm{e}$, to separate the effect of s/q and $T_\mathrm{i}/T_\mathrm{e}$. Qualitatively the analytical and experimental ratios show the following similar features: in the JET case, the maximum observed difference for $x > 0.5$ is predicted by equation (1), with no predicted difference (as in the observations) in the region of $x = 0.4$; for AUG, the increasing difference from 0.75 in towards the core is also predicted by equation (1). However, the observed

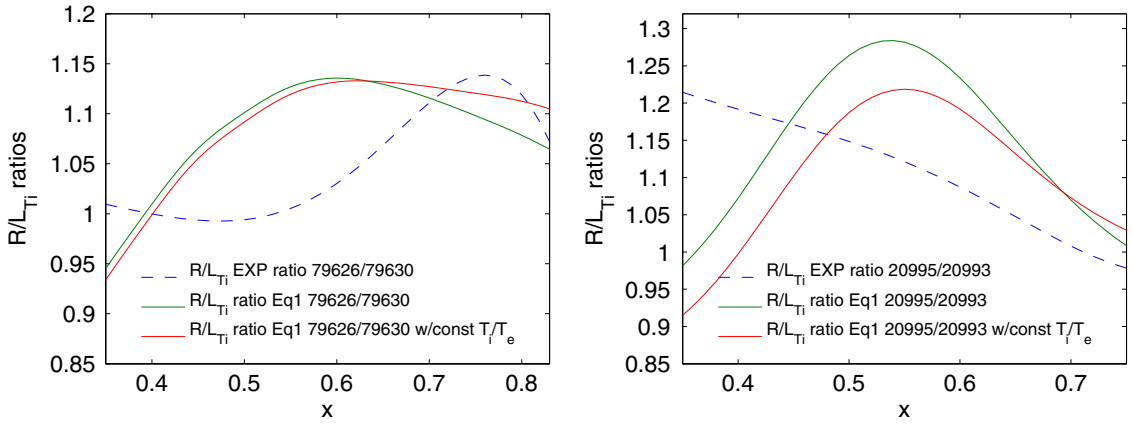

Figure 6. R/L_{T_i} experimental ratios compared with the analytical linear thresholds ratios (from equation (1)) for JET 79626/30 (left panel) and AUG 20993/95 (right panel).

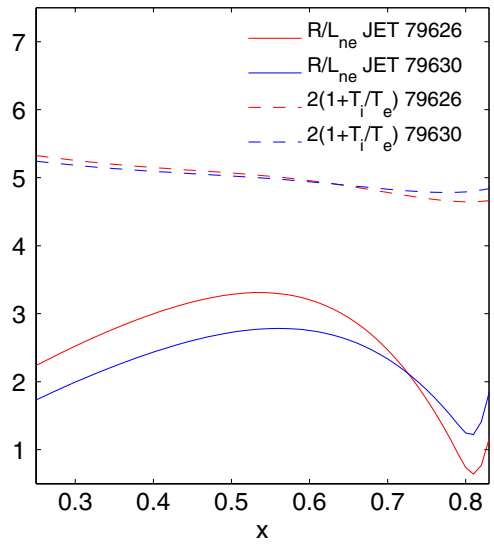

Figure 7. Comparison of R/L_{n_e} and $2(1 + T_i/T_e)$ in the JET pair of discharges for ascertaining the validity of the flat density limit applied in equation (1).

difference in the AUG case for $x < 0.5$, the low magnetic shear region ($s < 0.6$), is not predicted. The T_i/T_e component has a minor influence on the predicted R/L_{T_i} differences, as can be seen by comparing the curves with and without constant T_i/T_e. The differences between the analytical and experimental ratios can be either due to additional physics setting the transport, beyond ITG linear threshold physics, and/or due to the errors in the q-profiles identified with each discharge. Nevertheless, the correlations which are observed are encouraging with regard to isolating s/q as a significant factor in the observed core confinement differences within each pair of discharges. These analytical results are corroborated by numerical predictions by both GLF23 and QuaLiKiz, as outlined in the following sections.

3. Modelling tools and techniques

The core of CRONOS is a 1.5D transport solver, whereby 1D current diffusion, particle and energy equations are solved up to the separatrix, self-consistently with 2D magnetic equilibrium [25]. In this work, the NBI heat and current sources are calculated by NEMO/SPOT [38, 39]. The ICRH heat sources for the AUG discharges are calculated with PION [40]. The magnetic equilibrium is calculated with HELENA [41]. The neoclassical transport, bootstrap current, and neoclassical resistivity is calculated with NCLASS [42]. Turbulent transport is calculated with the GLF23 model [19, 26]. The fast particle profiles calculated by NEMO/SPOT and PION for NBI and ICRH are subtracted from the ion density profiles entered into GLF23. The calculated fast particle fractions for both the JET/AUG simulations successfully account for the observed differences in $\beta_N(W_{dia}/W_{mhd})$ and $\beta_N(W_{th})$.

For the JET simulations, GLF23 is employed within the region $x = 0$–0.83. For the AUG simulations, GLF23 is employed within the region $x = 0$–0.76. The simulations are carried out on the energy confinement timescale until the kinetic profiles reach stationary conditions. The background profiles and scalar quantities for the simulations are averaged over the time periods displayed in figure 1. Both *heat transport only* simulations (with prescribed density profiles for measurement) and *combined heat and particle transport* simulations are carried out. As mentioned in section 2, the JET input q-profiles are taken from CRONOS interpretative runs (current diffusion only simulations), and the AUG q-profile inputs from MSE measurements. For each discharge, comparison simulations were carried out substituting the q-profile input with the q-profile from the other member of each pair. The magnetic shear is then recalculated by CRONOS in a self-consistent manner. In such a manner GLF23 predicts the confinement difference solely due to the changed values of the q-profile and magnetic shear. Further linear threshold analysis examining the effect of s/q is also carried out with the quasilinear gyrokinetic transport model QuaLiKiz [28].

4. Results: GLF23 q-profile substitution simulations

In this section we isolate the degree of improved confinement which stems from the differences in q-profile between the two discharges in each pair, as according to the GLF23 model.

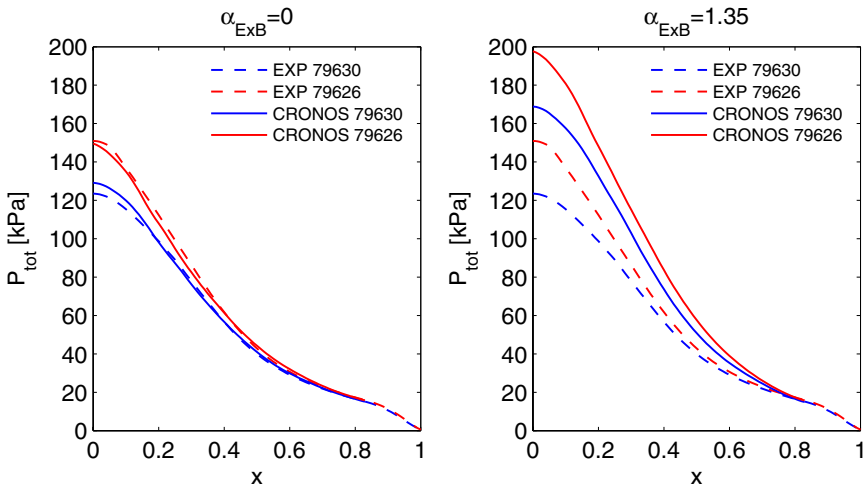

Figure 8. Results of combined heat and particle transport GLF23 simulations for JET 79630 and 79626. Predicted and observed $P_{\rm tot}$ profiles are compared with (right panel) and without (left panel) the inclusion of the full GLF23 $E \times B$ turbulence suppression model.

A comparison of full simulations with GLF23 of each separate discharge shows a similar degree of improvement in core confinement as observed. This is particularly the case for the JET discharges, as seen in figure 8, where the predicted total pressure is compared with the observations. Both with and without the GLF23 $E \times B$ turbulence suppression model (as specified by the $\alpha_{E\times B}$ parameter) the degree of predicted stored energy in 79626 is higher than that predicted for 79630 by a ratio comparable to the experimental observation. However, the main point of this work is to determine whether increased s/q in the outer radii of the improved confinement discharges is a significant factor responsible for the improved confinement through the increase in ITG linear thresholds. To this end, simulations for either JET 79630 or AUG 20995 were carried out substituting the q-profile of each simulation with the q-profile corresponding to the partner discharge in each pair. The comparison of simulations with differing q-profile inputs is the central point of this work. The details of these simulations are outlined in the following sections.

4.1. JET heat transport only

Figure 9 shows the $T_{\rm i}$ and $T_{\rm e}$ predictions for JET 79630. These simulations include *heat transport only*. Runs were carried out both with and without the GLF23 $E \times B$ turbulence suppression model. 79630 simulations with the substituted q-profile from 79626 (the improved confinement case) are also shown.

The inclusion of $E \times B$ suppression leads to overprediction of $T_{\rm i}$. This overprediction is also seen in JETTO [43] simulations of the same discharge, verifying that this observation is not an artefact of the CRONOS/GLF23 methodology used in this work. However, independently of the degree of prescribed $E \times B$ suppression, the q-profile substitution leads to a degree of $T_{\rm i}$ increase comparable to the experimentally observed difference between the two discharges. A more quantitative analysis of these differences, and of all subsequent simulations discussed below, can be found in the tables in section 4.5.

4.2. AUG heat transport only

The AUG simulations display a similar pattern to the JET simulations: simulations with the 20995 (improved confinement case) q-profile display improved ion confinement compared with a simulation which is identical apart from substituting in the 20993 q-profile. Inclusion of the $E \times B$ suppression model leads to $T_{\rm i}$ overprediction for both cases. This can be seen in figure 10. In the AUG 20993 case the general degree of $T_{\rm i}$ overprediction is more severe. However, regardless of the $E \times B$ suppression assumption, the q-profile substitution leads to a $T_{\rm i}$ difference qualitatively consistent with experimental observations.

4.3. JET combined heat and particle transport

In figure 11, the results of *combined heat and particle transport* simulations for JET 79630 are shown. The pattern remains similar to the heat transport only cases, although the primary effect of global confinement improvement following the q-profile substitution is now in the particle channel. R/L_n is increased at $x \gtrsim 0.4$ up until the GLF23 boundary condition at $x = 0.83$, while R/L_n is decreased for $x < 0.4$. Compared with the heat transport only case, the $T_{\rm i}$ profile increase is reduced when switching to the 79626 q-profile. This is due to the increased transport predicted by GLF23 due to the increased density gradients at $x > 0.4$, interpreted as the destabilization of TEM modes due to the propagation of the mode in the electron diamagnetic direction.

4.4. AUG combined heat and particle transport

The AUG heat and particle transport simulations show similar results to the JET heat and particle transport case. The AUG 20995 simulations are displayed in figure 12. For the AUG case, the degree of improved particle transport is consistent with observation, although when $E \times B$ suppression is included the $n_{\rm e}$ profiles are significantly higher than the measured values.

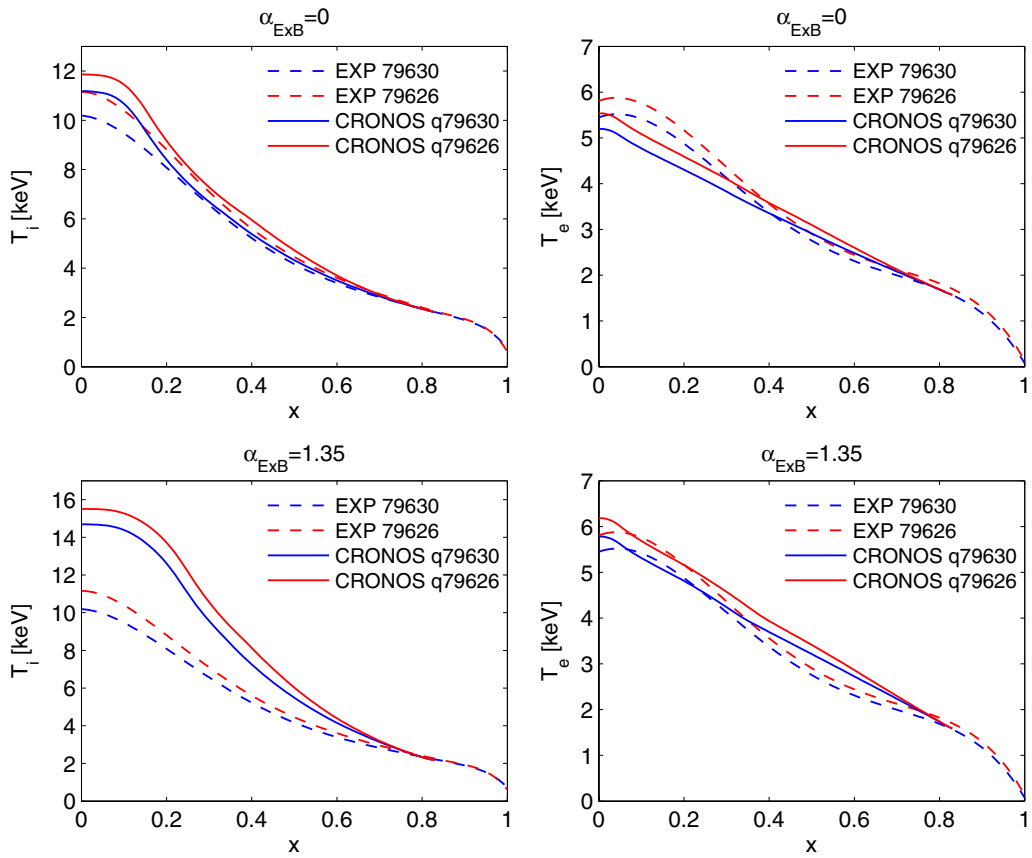

Figure 9. Results of heat transport only GLF23 simulations for JET 79630, comparing q-profile inputs from both 79630 and 79626. T_i profiles are on the left column. T_e profiles are on the right column. Results with both no $E \times B$ suppression (top row) and full $E \times B$ suppression (bottom row) are shown.

4.5. Summary of GLF23 runs

In tables 2 and 3, the simulation results are summarized in terms of the predicted core thermal energy content: $W_{\rm core} = \frac{3}{2}\int_0^{x_{\rm bc}}(P_{\rm th}(x) - P_{\rm th}(x_{\rm bc}))J\,{\rm d}x$. $P_{\rm th}$ is the thermal pressure. $x_{\rm bc}$ is taken at the GLF23 operational zone boundary at $x = 0.83/0.76$ for JET/AUG. J is the Jacobian corresponding to the volume element. The tables summarize—according to GLF23—the extent of the s/q effect *alone* in explaining the core confinement *differences* between each pair, both including and excluding $E \times B$ shear stabilization.

In spite of the absolute core energy content overprediction when including $E \times B$ shear stabilization, the degree of change when substituting the q-profile is maintained both with and without $E \times B$ shear stabilization. The degree of change also remains the same when including particle transport, due to the aforementioned increase in heat transport when increasing the density gradients. Taking the average of the GLF23 simulated core energy content for all runs, we obtain a ratio for 1.105 for the JET runs, and 1.17 for the AUG runs. This corresponds to the s/q effect *alone* contributing to 60% of the core confinement difference for the JET pair, and 35% of the core confinement difference in the AUG pair, according to GLF23. In section 5 we discuss other possible contributions to the core energy content differences.

4.6. Sensitivity of JET results to choice of $Z_{\rm eff}$ and $\alpha_{E\times B}$

The $Z_{\rm eff}$ taken for the JET simulations had an assumed form of $Z_{\rm eff} \propto n_e^{-0.4}$, and was normalized such that the line average $\langle Z_{\rm eff}\rangle$ agrees with bremsstrahlung measurements. However, as seen in figure 13, this assumption does not agree with $Z_{\rm eff}$ profiles calculated from carbon concentration measurements carried out by recombination charge-exchange spectroscopy (CX). For $x > 0.8$, where no CX measurements were available, an assumed near constant CX $Z_{\rm eff}$ profile was prescribed.

The sensitivity of the calculated q-profile to $Z_{\rm eff}$ was examined by repeating the interpretative run for 79630 with alternative $Z_{\rm eff}$ profiles based on the discrepancy between the Bremsstrahlung and CX measurements. Since the CX measurements were only available following application of the neutral beam injection, neither precise information on the $Z_{\rm eff}$ profile shape in the early phase of the discharge nor an alternative value of $\langle Z_{\rm eff}\rangle$ was available. Therefore, we tested the sensitivity by simply assuming a $Z_{\rm eff}$ profile identical to the CX profile from figure 13, and reducing $\langle Z_{\rm eff}\rangle$ in the interpretative run by a constant factor $\sim$1.3, typical of the discrepancy between the bremsstrahlung and CX measurements.

The impact of using the CX $Z_{\rm eff}$ profile in the GLF23 simulations was also examined. Both the 79630 heat transport only and combined heat and particle transport simulations were

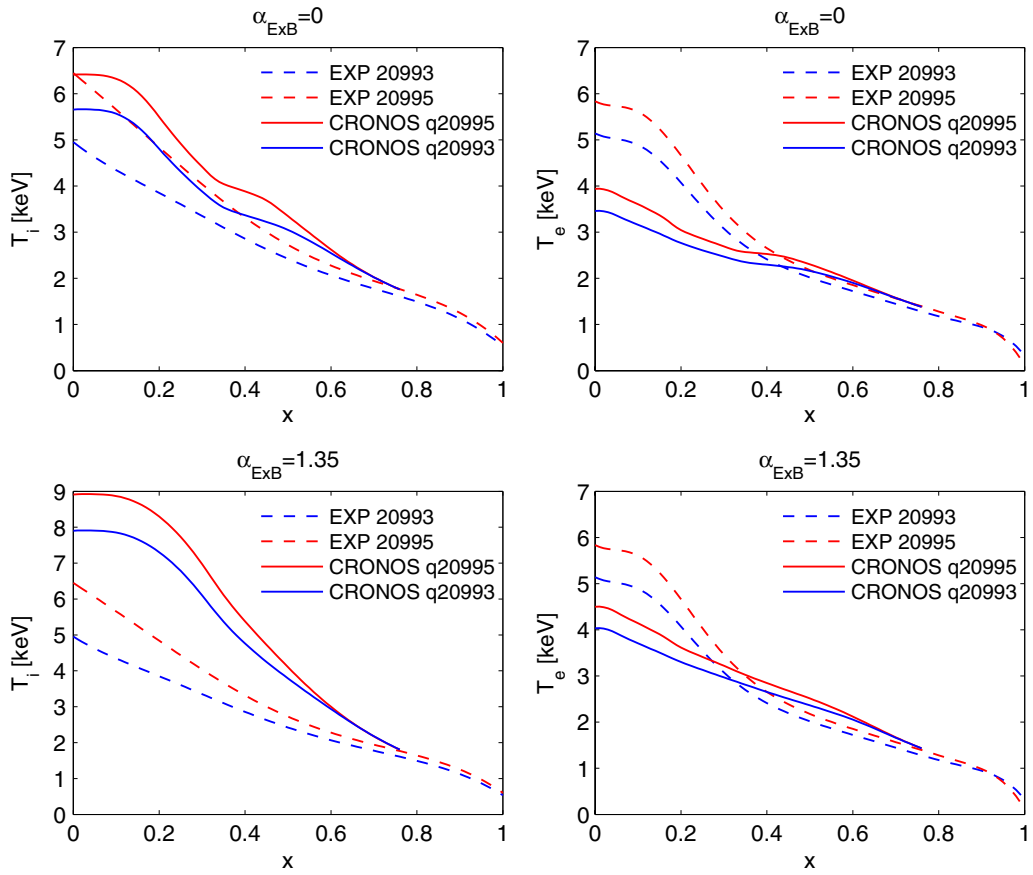

Figure 10. Results of heat transport only GLF23 simulations for AUG 20995, comparing q-profile inputs from both 20995 and 20993. T_i profiles are in the left column. T_e profiles are in the right column. Results with both no $E \times B$ suppression (top row) and full $E \times B$ suppression (bottom row) are shown.

repeated using CX Z_eff profiles averaged over the 7.14–7.64 s time window. Finally, the same simulations were repeated when reducing the GLF23 $\alpha_{E\times B}$ parameter to 1. The heat transport only results are seen in figure 14, and the combined heat and particle transport results in figure 15.

The q-profile sensitivity to the Z_eff profile, within the range studied, is small. However, the variation of the T_i predictions when switching to the CX measured Z_eff profile is not negligible, and is primarily due to reduced dilution. When combined with switching to $\alpha_{E\times B} = 1$, the ion temperature overprediction, while still apparent, is significantly diminished. This more minor level of T_i overprediction is consistent with GLF23 results reported in [44], where both CX Z_eff profiles and $\alpha_{E\times B} = 1$ were employed. Also in the combined heat and particle transport case, the degree of averaged n_e overprediction is reduced when switching to the CX Z_eff profile, although the profile peaking still remains well above the experimentally observed value. We reiterate that the relative differences due to the s/q effect—the central point of this work—are invariant to the choice of Z_eff and $\alpha_{E\times B}$.

4.7. Discussion of GLF23 $E \times B$ suppresion model

The absolute W_core values are significantly overpredicted when including $E \times B$ shear suppression in the GLF23 model. It is difficult to determine whether this overprediction is due to a deficiency in the $E \times B$ suppression model, or due to an intrinsic overprediction of the underlying instability thresholds. We note that GLF23 simulations for high triangularity JET hybrids also display a similar T_i overprediction as seen in this work [45]. However, in previous work, the JET hybrid discharge 58323 was shown to be satisfactorily predicted by GLF23 [46], even when including $E \times B$ suppression. Similar satisfactory predictions of JET hybrid discharges have also been reported previously [47]. A simulation of discharge 58323 was repeated with the same CRONOS/GLF23 methodology performed in this work, and the previous result was indeed recovered. However, additional simulations taking into account the uncertainties in Z_eff, combined with the resultant differences in the modelled q-profile, also led to T_i overpredictions as seen here. For other JET discharges analysed in [46], numerous examples of significant T_i deviations can be seen in figure 4 of that paper. Also in this work, the degree of overprediction—while still significant—is reduced when using the Z_eff profile from charge-exchange measurements as shown in section 4.6.

These results highlight the modelling sensitivity to the input parameters, which helps explain the scatter in the literature with regard to the degree of predicted GLF23 T_i overprediction. We also note that in recent TGLF [48] modelling of DIII-D hybrid discharges [49], T_i was reported

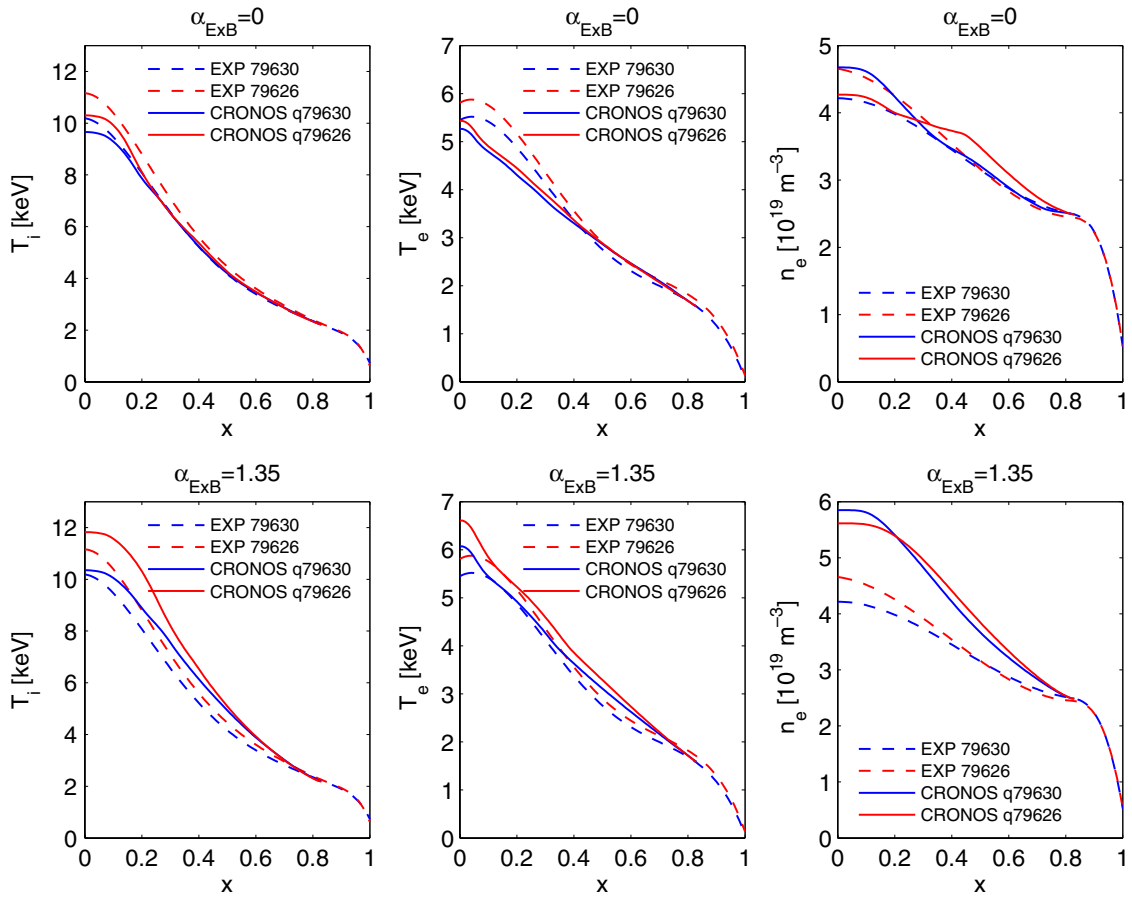

Figure 11. Results of combined heat and particle transport GLF23 simulations for JET 79630, comparing q-profile inputs from both 79630 and 79626. T_i profiles are in the left column. T_e profiles are in the centre column. n_e profiles are in the right column. Results with both no $E \times B$ suppression (top row) and full $E \times B$ suppression (bottom row) are shown.

to be significantly underpredicted when not employing $E \times B$ suppression. However, the ion energy transport was reported to be reduced to neoclassical levels, while the neoclassical transport was taken from a modified Chang–Hinton model. This model yields diffusivities larger than that calculated by first-principle methods such as by the NCLASS [42] model employed in this work. This may lead to more pessimistic T_i predictions. Further validation of the various transport models on discharges from different machines, while employing the same modelling methodology to reduce scatter induced by different modelling assumptions, would be highly beneficial.

With regard to potential explanations for a deficiency in the GLF23 $E \times B$ suppression model, we note that discharges considered here are highly NBI-driven discharges, with a relatively high degree of rotational shear. It has been shown that due to parallel velocity shear the efficiency of $E \times B$ shear in decreasing transport decreases at high rotation [50–52]. This may be relevant also for the increased q_{95} hybrid discharges. At higher q, the parallel (to the field line) component of the toroidal velocity is increased. While parallel velocity shear destabilization is included in GLF23, the destabilization effect is minor for the rotation velocities considered here. This is seen by comparing JET 79630 GLF23 T_i predictions (with heat transport only), for cases where the $E \times B$ suppression model is not included ($\alpha_{E\times B} = 0$), and where the toroidal velocity itself is set to zero ($V_\mathrm{tor} = 0$). The difference between the predictions corresponds to the parallel velocity shear destabilization, which in this case only reduces the T_i profile by $\sim$2%. However, it would be worthwhile to reexamine the effect of parallel velocity gradient destabilization with gyrokinetic codes at experimentally relevant levels of turbulent fluxes for improved transport model verification.

Recent results at JET show that the effect of rotational shear in increasing R/L_{T_i} (due to decreased stiffness) is located only in the low magnetic shear region, in our case $x < 0.4$ [17, 18]. However, this is inconsistent with the main effect of including GLF23 $E \times B$ suppression in our simulations, which increases R/L_{T_i} primarily in the high magnetic shear region $x > 0.5$. Additionally, other recent JET results show that R/L_{T_i} in $x > 0.5$ does not vary with the NB/IC heating mix, at constant total power, even if the rotation profiles vary significantly [53]. This is corroborated by previous analysis of an AUG improved H-mode discharge [36], where core R/L_{T_i} was not observed to increase following a significant increase in NBI power during the discharge, which led to increased rotation. Furthermore, analysis of the same discharge with the Weiland model [54] predicted no significant improvement in core confinement due to rotation.

A further uncertainty in the modelling of the $E \times B$ shear is the contribution of the poloidal rotation. We have neglected

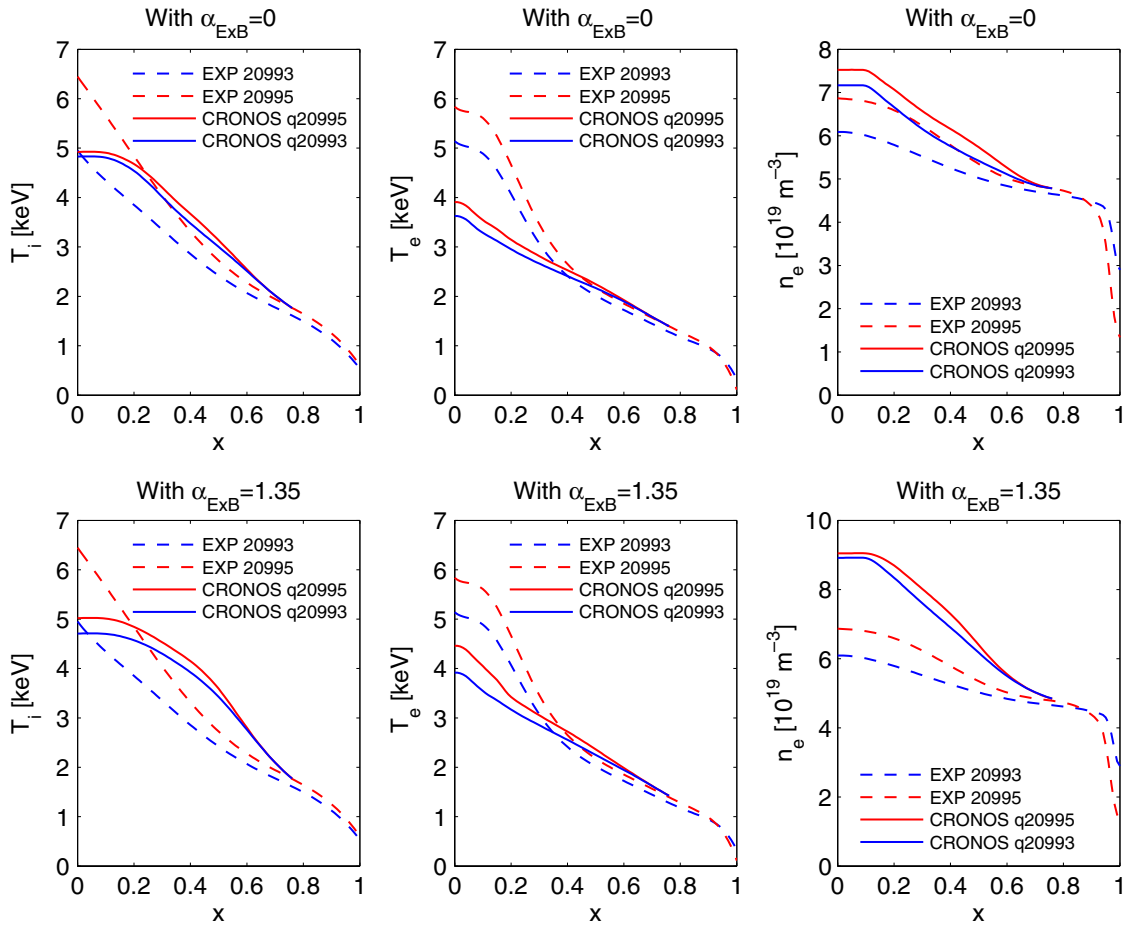

Figure 12. Results of combined heat and particle transport GLF23 simulations for AUG 20995, comparing q-profile inputs from both 20995 and 20993. T_i profiles are in the left column. T_e profiles are in the centre column. n_e profiles are in the right column. Results with both no $E \times B$ suppression (top row) and full $E \times B$ suppression (bottom row) are shown.

Table 2. Core thermal energy following GLF23 predictions for JET hybrids. Units are (MJ).

		Heat transport		Heat and particle	
	EXP	No $E \times B$	With $E \times B$	No $E \times B$	With $E \times B$
79630 (q30)	1.67	1.71	2.37	1.71	2.68
79630 (q26)	1.97	1.9	2.62	1.83	3.03
Ratio	1.17	1.11	1.11	1.07	1.13

Table 3. Core thermal energy following GLF23 predictions for AUG hybrids. Units are (MJ).

		Heat transport		Heat and particle	
	EXP	No $E \times B$	With $E \times B$	No $E \times B$	With $E \times B$
20995 (q93)	0.2	0.249	0.367	0.255	0.371
20995 (q95)	0.294	0.293	0.421	0.3	0.429
Ratio	1.47	1.18	1.15	1.18	1.16

the neoclassical poloidal rotation in our calculation of the radial electric field, as it is negligible compared with the NBI-driven toroidal rotation. However, measurements in DIII-D QH-mode discharges show a discrepancy in both magnitude and sign of impurity poloidal rotation velocities compared with the neoclassical expectation [55]. At JET, measurements have shown poloidal rotation velocities greater than the neoclassical expectation in the vicinity of internal transport barriers, while the measurements and neoclassical predictions agree outside of the ITB region [56]. In measurements at MAST, no significant disagreement between the poloidal rotation neoclassical prediction and measurements was found, although it has been suggested that at low aspect ratio the neoclassical damping of poloidal rotation may be stronger

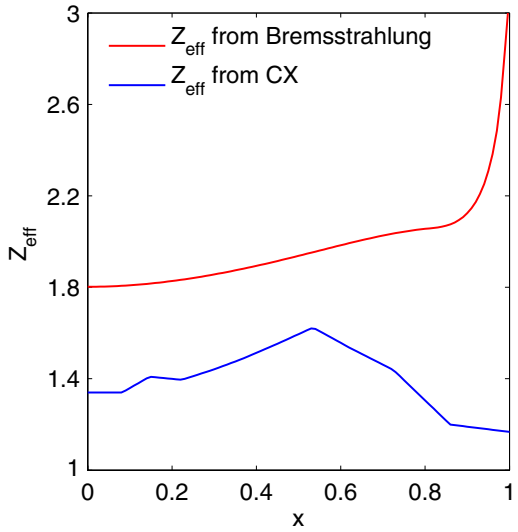

Figure 13. Comparison of $Z_{\rm eff}$ profiles for JET 79630 averaged between 7.14 and 7.64 s, both from line-averaged bremsstrahlung and an assumed profile, and from carbon concentration CX measurements.

compared with at high aspect ratio [57]. There is still no clear consensus regarding the conditions necessary for the onset of non-neoclassical poloidal rotation and its degree of magnitude when existent. However, in light of these previous results it is possible that the discharges considered in this work may contain non-negligible anomalous poloidal rotation. No measurements are available in these specific discharges to shed light on this question. Nevertheless, anomalous poloidal rotation could reduce the magnitude of the radial electric field, reducing the degree of $E \times B$ turbulence suppression, partly explaining the discrepancy observed in the simulations.

The question of how to model and predict the effect of rotation on transport is thus still an open one. Nevertheless, the central point of this work is to verify the *relative* effect of the q-profile in leading to the difference in $W_{\rm core}$ between the two shots within each pair. This effect is independent of the $E \times B$ turbulence suppression model.

5. Additional contributions to core confinement differences

In this section we explore possibilities—other than the s/q effect—for explaining the observed differences in core confinement for both the JET and AUG pairs.

5.1. Density profiles

For the heat transport only simulations, the prescribed density profile may have an effect on the predicted core confinement. This may be due to both the inherent different stored energy content, and also the R/L_n parametrization of the predicted transport. In figure 16 a comparison of AUG 20995 heat transport simulations prescribing both the 20995 and 20993 density profiles is displayed. This sensitivity test was carried out for AUG since the $\overline{n}$ difference for the AUG pair is greater than the JET pair: 6% as opposed to 3%.

The resulting difference in $W_{\rm core}$ is a negligible <1% increase when prescribing the 20993 $n_{\rm e}$ profile as opposed to the 20995 profile, for the no $E \times B$ suppression case. The increase in $T_{\rm i,e}$ compensates for the decreased $n_{\rm e,i}$ profiles. For the full $E \times B$ suppression case, prescribing the 20993 $n_{\rm e}$ profile led to a 6% *decrease* in $W_{\rm core}$. The discrepancy between the two cases can be traced to the flat temperature profiles in the 20995 $n_{\rm e}$ case located at $x = 0.4$. This is an artefact of GLF23 modelling, where typically above a certain R/L_n threshold the sensitivity of the transport to R/L_n increases considerably. Evidently the 20995 R/L_n is at that threshold around $x = 0.4$. However, these TEM modes, which leads to a flat temperature profile in the region of $x = 0.4$ in the $\alpha_{E\times B} = 0$ case, are stabilized by the $E \times B$ suppression model when $\alpha_{E\times B} = 1.35$. Thus the flat temperature profile in the $x = 0.4$ region in the $\alpha_{E\times B} = 0$ case is not evident in the $\alpha_{E\times B} = 1.35$ case.

5.2. $Z_{\rm eff}$

Sensitivity of the transport to $Z_{\rm eff}$ is examined for the JET pair, which displays a greater difference in measured $\langle Z_{\rm eff}\rangle$ compared with the AUG case: 12% as opposed to 3%. The improved confinement discharge has lower $\langle Z_{\rm eff}\rangle$ in both pairs. In figure 17 two separate JET 79630 simulations are compared, with the differing $Z_{\rm eff}$ profiles. The simulations include both particle and heat transport, and no $E \times B$ suppression is included in these simulations. The results show that the sensitivity is small but not entirely negligible: the 79626 $Z_{\rm eff}$ case has an increased $W_{\rm core}$ by 4% compared with the 79630 $Z_{\rm eff}$ case, which is also in the correct direction of the experimentally observed improvement.

5.3. Heat and particle sources

Simulations which compare the effect of substituting only the heat and particle source profiles were carried out, to test the sensitivity of the predicted core energy content on the precise source profiles. This was done by re-running the combined heat and particle transport simulation of 79630 with the 79626 q-profile, and replacing the heat and particle sources in the simulation with those calculated in the 79626 interpretative simulation. However, due to the highly stiff nature of the GLF23 model, the predicted changes in $W_{\rm core}$ following such substitutions were completely negligible (<1%).

5.4. GLF23 boundary conditions

The largest part of the observed difference in confinement between each pair of discharges is from the core. However, the differences in the values of the kinetic profiles at the GLF23 boundary conditions—$x = 0.83$ for the JET pair and $x = 0.76$ for the AUG pair—can still play a significant role. To test the impact of the boundary condition on the core confinement, we first note that from the definition of the gradient length $1/L_T = \frac{{\rm d}T/{\rm d}r}{T}$, we can obtain $T(r) = T(r_{\rm bc})\exp(\int_{r_{\rm bc}}^{r} 1/L_T(r)\,{\rm d}r)$, where we have taken a temperature gradient length for this example, and $r_{\rm bc}$ is the boundary condition radius. If we then assume that the inverse gradient lengths of the kinetic profiles would be maintained following slight changes in

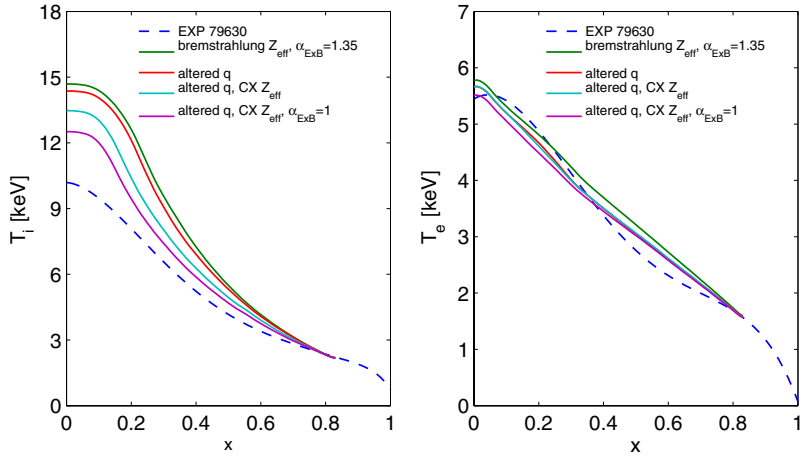

Figure 14. Results of heat transport GLF23 simulations for JET 79630, testing the sensitivity of the results to $Z_{\rm eff}$ and the $\alpha_{E\times B}$ parameter. Progressive results for $T_{\rm i}$ (left panel) and $T_{\rm e}$ (right panel) are shown where the experimental profile is compared with the original 79630 simulation with bremsstrahlung $Z_{\rm eff}$ and $\alpha_{E\times B} = 1.35$, a simulation where the q-profile is substituted with the q-profile obtained with lowered $Z_{\rm eff}$ profiles, additionally reducing $Z_{\rm eff}$ itself in the predictive simulation to the CX measured $Z_{\rm eff}$ profile, and finally additionally switching the $\alpha_{E\times B}$ parameter to 1.

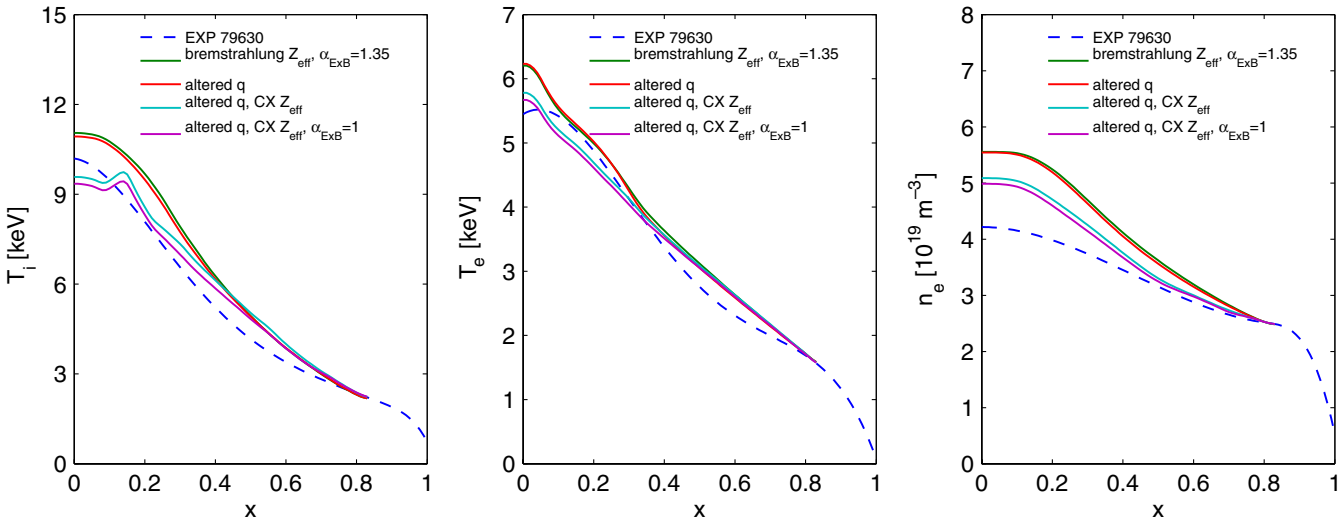

Figure 15. Results of combined heat and particle transport GLF23 simulations for JET 79630, testing the sensitivity of the results to $Z_{\rm eff}$ and the $\alpha_{E\times B}$ parameter. Progressive results for $T_{\rm i}$ (left panel), $T_{\rm e}$ (centre panel) and $n_{\rm e}$ (right panel) are shown where the experimental profile is compared with the original 79630 simulation with bremsstrahlung $Z_{\rm eff}$ and $\alpha_{E\times B} = 1.35$, a simulation where the q-profile is substituted with the q-profile obtained with lowered $Z_{\rm eff}$ profiles, additionally reducing $Z_{\rm eff}$ itself in the predictive simulation to the CX measured $Z_{\rm eff}$ profile, and finally additionally switching the $\alpha_{E\times B}$ parameter to 1.

the boundary condition values, then the modification of the kinetic profiles following a change in the boundary conditions can be calculated by a simple multiplication of each profile corresponding to the change in each respective boundary condition value. In such a case, the effect of these boundary conditions on the core confinement can be easily examined. We can recalculate the experimental $W_{\rm core}$ by simply multiplying the experimental kinetic profiles by factors corresponding to the ratios of the boundary conditions between the discharges in each pair. This assumption was tested with GLF23 simulations, and was found to be adequate.

The 79630 experimental kinetic profiles were multiplied to match the 79626 boundary conditions, and $W_{\rm core}$ recalculated. The recalculated $W_{\rm core}$ was 5% higher than the original $W_{\rm core}$. Thus, the boundary conditions alone may be responsible for ∼30% of the perceived core confinement difference. For the AUG case, setting the 20993 experimental kinetic profiles to the 20995 boundary conditions showed that ∼25% of the perceived core confinement difference may be due to the boundary conditions.

5.5. NTM effect

While the pair of JET discharges do not have any NTMs within the temporal period of analysis, AUG 20993 (the lowered confinement case) has a low amplitude 3/2 NTM located in the vicinity of $x = 0.5$, in accordance with the location of $q = 1.5$ [31]. It is possible that the effect of this NTM on the kinetic profiles can explain part of the 40% difference in $W_{\rm core}$ for the AUG pair which remains after taking into account

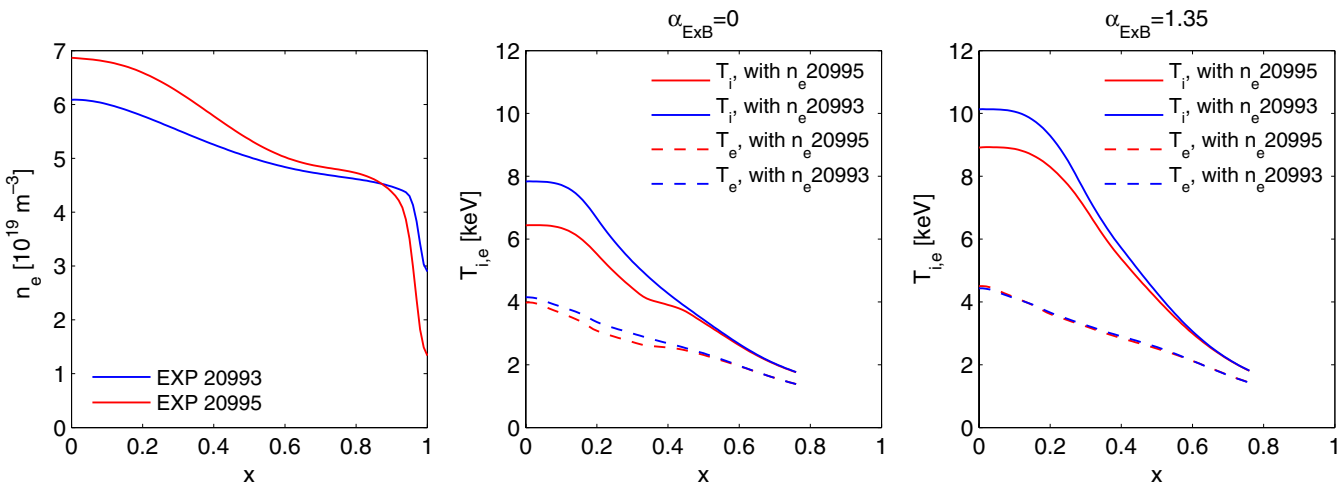

Figure 16. Comparison of AUG 20995 heat transport simulation with GLF23, with different prescribed n_e profiles. The dashed lines correspond to T_e, and the solid lines to T_i. The prescribed n_e profiles are seen in the left panel, the temperature profiles without $E \times B$ suppresion in the centre panel, and the temperature profiles with full $E \times B$ suppresion in the right panel.

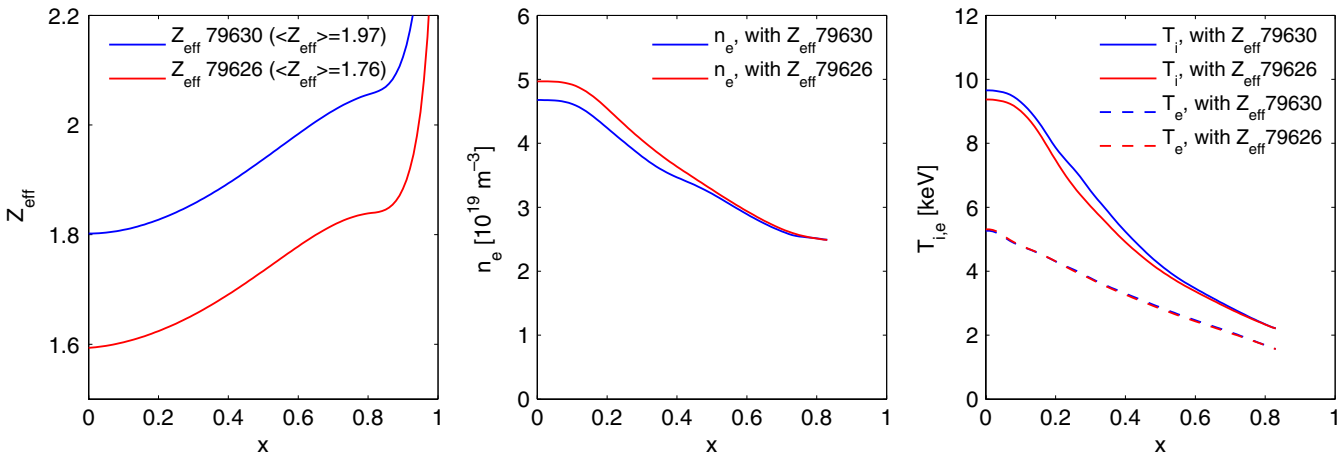

Figure 17. Comparison of JET 79630 combined particle and heat transport simulation with GLF23, without $E \times B$ suppression. The dashed lines correspond to simulations with Z_{eff} from 79630, and the solid lines to Z_{eff} from 79626. The prescribed Z_{eff} profiles are seen in the left panel, the density profiles in the centre panel, and the temperature profiles in the right panel.

the s/q effect and the boundary condition effect. While it is difficult to precisely measure the impact of this NTM on confinement, we estimate the maximum possible impact of NTM as follows. The experimental T_e of the two AUG discharges are compared (figure 18), where the 20995 profile is normalized to have the same boundary condition as 20993 at $x = 0.76$. We can see that the T_e differences following the normalization are indeed localized to the region $x < 0.5$, in line with a possible relation to the NTM activity. The ratio between the profiles is also seen in figure 18. To estimate the effect of the NTM on the total W_{core}, we make a strong assumption that these T_e differences are fully due to the NTM, and not due to the differing q-profile and rotation profiles. We can then assess the potential impact of the NTM on W_{core} by multiplying all kinetic profiles ($T_{i,e}$, $n_{i,e}$) of discharge 20993 by the ratio seen in the right panel of figure 18 for $x < 0.5$, and then recalculate W_{core}. This led to a W_{core} increase of 20993 of 17% of the total difference between 20993 and 20995. We can thus conclude that while the NTM may have a non-negligible impact on core confinement, the impact is not large enough to fully explain the remaining 40% difference.

5.6. Predictions in the low magnetic shear region

In figure 19 we compare the predicted R/L_{T_i} profiles from the GLF23 simulations with the observed values, for both pairs of discharges. The results shown are from simulations including heat transport only, and the results both with and without $E \times B$ suppression are shown. The absolute predictions—particularly when including $E \times B$ suppression—deviate from the observations. However, the relative predictions—when substituting the q-profile—approximately agree with the observations in the region $x > 0.4$.

In the JET case, the location of the R/L_{T_i} differences when substituting the q-profile agrees with the location of the s/q differences, as seen in figure 2. The location of these differences also fully agrees with the observations. For the AUG pair, this is also the case for $x > 0.4$, but the

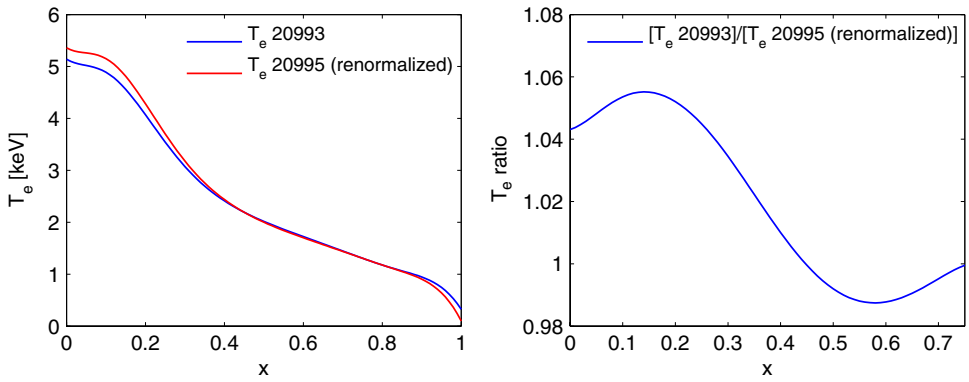

Figure 18. Comparison of AUG 20993 and 20995 T_e profiles, with the 20995 profile normalized to the 20993 GLF23 boundary condition at $x = 0.76$. The T_e profiles themselves are seen in the left panel, and the ratio between the profiles in the right panel.

observed differences in R/L_{T_i} within the region $x < 0.4$ are not predicted by GLF23. This region corresponds to the low magnetic shear region ($s < 0.6$). Note that in the $\alpha_{E\times B} = 0$ AUG case, the dip of R/L_{T_i} at around $x = 0.4$ is due to the density gradient exceeding a threshold beyond which transport is considerably increased in GLF23. When replacing the density profiles with the 20993 profiles, this dip is not seen, but the relative differences in R/L_{T_i} when substituting the q-profile are maintained. When including $E \times B$ shear in the AUG case, the predicted R/L_{T_i} differences slightly increase in the $x = 0.4$ region. This is due to the difference in rotation profiles, also seen in figure 2. However, this is still insufficient to explain the observed R/L_{T_i} differences for $x < 0.4$, which contributes to the observed $W_{\rm core}$ difference between AUG 20993/20995. A further proportion of the $W_{\rm core}$ difference in the AUG pair thus comes from the low magnetic shear region, a difference which is not predicted by GLF23.

6. QuaLiKiz linear threshold analysis

Additional analysis was carried out for both the JET and AUG cases with QuaLiKiz, where we assess the sensitivity of the instability linear thresholds to the q-profile, at the locations $x = 0.35, 0.45, 0.55, 0.65, 0.75$. This was carried out by a QuaLiKiz R/L_{T_i} scan, to identify the linear threshold. The QuaLiKiz calculations took as input the parameters for 79630 for the JET pair, and 20995 for the AUG pair. The simulation at each radial point was then repeated after replacing q and s with the values from 79626 and 20993, respectively. The results are seen in figure 20. The QuaLiKiz results are compared with the experimental R/L_{T_i} calculated with respect to a radial coordinate defined as $(R_{\rm in} + R_{\rm out})/2$, where $R_{\rm in,out}$ are the radii to the high-field and low-field side flux surfaces on the midplane. R/L_{T_e} was kept at the observed ratio to R/L_{T_i} throughout the QuaLiKiz R/L_T scans.

While the predicted relative differences in R/L_{T_i} are recovered following the q-profile substitution—particularly for JET—the absolute values for $x > 0.5$ are overpredicted. However, both QuaLiKiz and GLF23 utilize $s - \alpha$ geometry, only correct in a circular small inverse aspect ratio limit. Shaped geometry can have a significant impact on the linear threshold calculation. A parametrization of this effect has been obtained from an extensive study of ETG linear thresholds from linear gyrokinetic calculations, which included shaping [58]. The study assumed adiabatic ions. The obtained (from fitting) ETG linear threshold formula is thus isomorphic to the ITG case assuming adiabatic electrons, which we rewrite as follows:

$$(R/L_{T_i})_c = \max\left\{(1 + T_i/T_e)\left(1.33 + 1.91\frac{s}{q}q\right)(1 - 1.5\epsilon)\right.$$
$$\left.\times[1 + 0.3\epsilon(\mathrm{d}\kappa/\mathrm{d}\epsilon)], 0.8R/L_n\right\} \quad (3)$$

where $\epsilon = r/R$ and κ is the elongation. Equation (3) is very similar to equation (1) apart from the increased weight of s/q, and the geometrical terms. These terms are of more importance at higher radii.

We estimate the effect of shaped geometry by multiplying the QuaLiKiz calculated R/L_{T_i} by the geometrical term $(1 - 1.5\epsilon) \times [1 + 0.3\epsilon(\mathrm{d}\kappa/\mathrm{d}\epsilon)]$ from equation (3). The results are seen in figure 21. The predicted and observed R/L_{T_i} are now reconciled for $x > 0.5$, particularly for the JET cases. The measured R/L_{T_i} at $x < 0.5$ remain far from threshold. However, this is consistent with observations in JET plasmas with high rotational shear, where R/L_{T_i} at greater radii have been measured to be tied close to the linear threshold, while at lower radii (low magnetic shear) the profile stiffness can be significantly reduced [17].

We note that agreement between the QuaLiKiz predictions and the measured R/L_{T_i} for $x > 0.5$ can be improved to the same degree as seen in figure 21 by simply setting as input the experimental gradients with respect to $R_{\rm out}$ as opposed to $(R_{\rm in} + R_{\rm out})/2$. This may reflect the following physics: at high magnetic shear—characteristic of hybrid scenarios for $x > 0.5$—the ITG modes are more strongly ballooned to the low-field side due to the increased ion Landau damping. We speculate here that in such situations, it may thus be more appropriate to input experimental gradients defined with $R = R_{\rm out}$ into the model, i.e. the gradient in the region where the mode is most unstable. This topic, as well as profile stiffness at low magnetic shear, is currently under investigation as part of the ongoing development of the QuaLiKiz transport model.

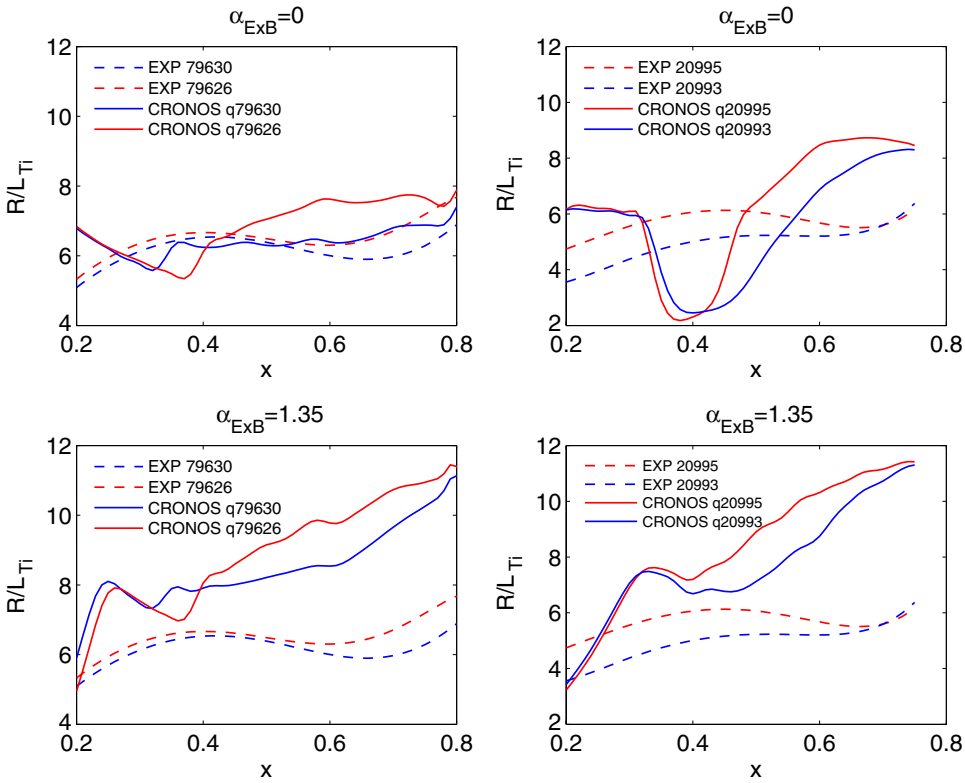

Figure 19. Comparison of R/L_{T_i} GLF23 predictions following q-profile substitution. Results are shown for the JET pair (left column) and the AUG pair (right column) both with (upper row) and without (lower row) the inclusion of $E \times B$ suppresion.

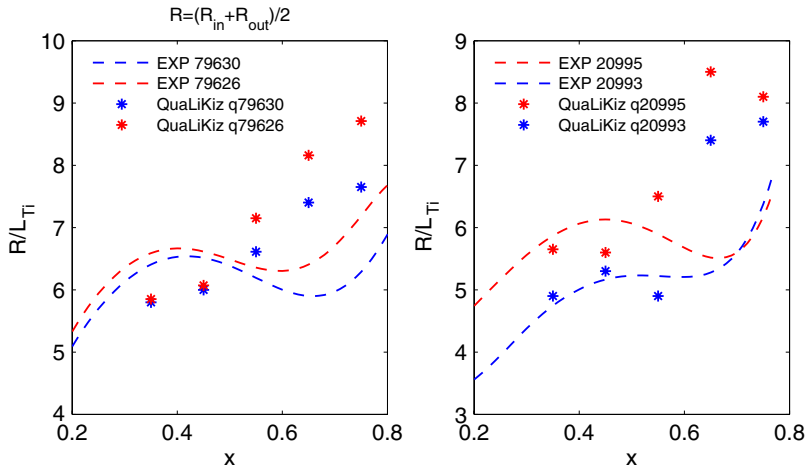

Figure 20. Comparison of R/L_{T_i} QuaLiKiz predictions following q-profile substitution. Results are shown for the JET pair (left panel) and the AUG pair (right panel).

In summary, QuaLiKiz linear threshold calculations following q-profile substitution show that the s/q differences between each pair of discharges is responsible for a significant degree of the observed R/L_{T_i} differences. This is in corroboration with the GLF23 results. However, the significant overprediction of R/L_{T_i} for $x > 0.5$ may be a symptom of the well-known limitation of applying $s - \alpha$ geometry in shaped plasmas. An estimation of the shaping effect, utilizing previous linear gyrokinetic calculations which included shaping, led to a reconciliation between the predicted and observed R/L_{T_i} values for $x > 0.5$, particularly in the JET case. This is consistent with the observation that even with no $E \times B$ shear included ($\alpha_{E\times B} = 0$), also the GLF23 model overpredicts R/L_{T_i} for $x > 0.5$ as seen in figure 17.

7. Conclusions

7.1. JET 79630/79626 q-profile substitution

A significant proportion of the core confinement difference between the JET hybrid scenarios analysed here is due to an increase in the ITG threshold due to improved q-profile shaping in the high magnetic shear region, at $x > 0.4$, according to GLF23. A proportion of ~60% of the observed improvement

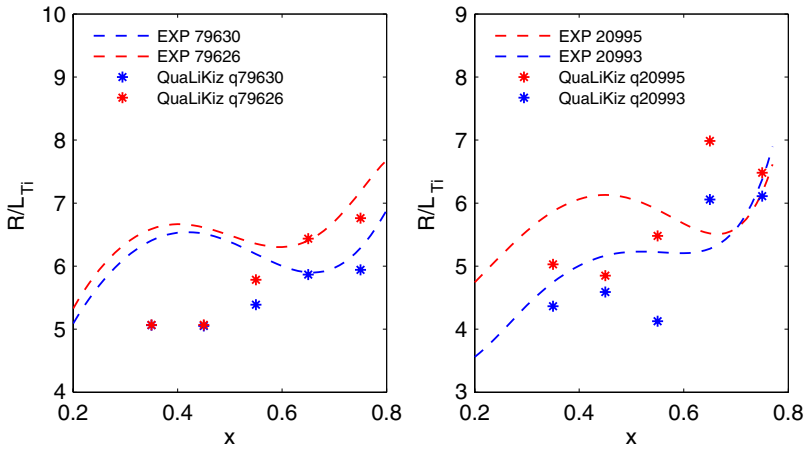

Figure 21. Comparison of R/L_{T_i} QuaLiKiz predictions following q-profile substitution. Results are shown for the JET pair (left panel) and the AUG pair (right panel). The QuaLiKiz predictions here have been multiplied by the geometrical factor from equation (3) to estimate the effect of shaping on the linear thresholds.

in core is predicted through q-profile substitution alone. In the heat transport simulations, differences in R/L_{T_i} are in the JET case only observed in the high magnetic shear region ($x > 0.4$) and are correlated with differences in s/q. This relative difference in W_{core} is independent of the inclusion of the $E \times B$ suppression model in GLF23. In the combined heat and particle simulations, the primary channel of confinement improvement is n_e. The majority of the remaining 40% of core confinement difference can be linked to the differences in GLF23 boundary conditions at $x = 0.83$. Slight differences in n_e and Z_{eff} between the shots can account for the remaining proportion.

7.2. AUG 20995/20993 q-profile substitution

In the AUG hybrid scenarios analysed, approximately ~60% of the observed W_{core} difference can be accounted for by a combination of the s/q effect (35%) and the difference in boundary conditions (~25%). Again, this is independent of the $E \times B$ suppression model. It has been estimated that the NTM in 20933 may be responsible for up to a further ~20% of the difference. As in the JET case, the improvement due to the s/q effect is predicted to be primarily in the particle channel when including particle transport in GLF23. The observed R/L_{T_i} differences occur both in the low- and high-magnetic shear regions within $x = 0.2$–0.6. The R/L_{T_i} difference in the high-shear region is correlated with a difference in s/q. However, the difference in the low-shear region cannot be explained by s/q effects, according to GLF23. Due to the difference in rotational shear for $x < 0.4$ between the two discharges in the AUG case (see figure 2), it may be possible that reduced stiffness in the low-shear region (not predicted by the stiff GLF23) may account for a further proportion of core confinement difference, as also observed in JET [17, 18]. It is possible that the low amplitude NTM present in 20993 at around $x = 0.5$ is responsible for a slight local difference in observed R/L_{T_i} in the $x = 0.5$ region. However, the NTM cannot explain the observed differences in R/L_{T_i} for $x < 0.4$.

7.3. GLF23 E × B suppression model W_{core} overprediction

The overprediction of W_{core} in GLF23 when including the full $E \times B$ suppression model opens up questions regarding the appropriate value of $\alpha_{E\times B}$ for use in GLF23, accuracy of Z_{eff} for modelling input, accuracy of the GLF23 parallel velocity shear destabilization model, the mechanism of $E \times B$ shear suppression (threshold shift versus stiffness reduction), and the possible role of anomalous poloidal rotation. However, in addition the intrinsic linear thresholds are overpredicted by the GLF23 $s - \alpha$ model. Finite aspect ratio and elongation effects reduce the predicted linear thresholds. This then would reduce the degree of apparent overprediction from the $E \times B$ model. However, the critical point is that the degree of core confinement improvement due to s/q is *independent* of both shaping effects and the value of $\alpha_{E\times B}$. Our conclusions that derive from q-profile shaping effects are thus independent of the above-mentioned modelling uncertainties, while these results simultaneously underline the challenges raised by these same uncertainties.

7.4. Final conclusions

The majority of the W_{core} *differences* can be satisfactorily predicted regardless of the $E \times B$ model, and the s/q profile plays a significant role in these predictions. These GLF23 predictions are also corroborated by R/L_{T_i} threshold analysis using QuaLiKiz. A general caveat is that the relatively low magnitude of the experimentally observed and calculated differences in both R/L_{T_i} and the q-profile demands that these conclusions be treated with caution. The small magnitude of the effect—a H_{98} increase of up to ~0.1 due to s/q only—hinders the experimental isolation of the s/q impact which can be in general be easily masked by competing effects and experimental error. Nevertheless, the results obtained here are consistent with the theoretically expected impact of q-profile shaping on core confinement through threshold increase at outer radii and provides an encouraging validation in this regard. In ITER operational scenario studies, such H_{98} improvements of up to ~0.1 due to q-profile shaping have in

fact been shown to have a significant impact on the projected fusion power in the ITER hybrid scenario [29]. Validation of these ITER predictions made with GLF23 was the initial driving motivation for this work. Further q-profile shaping experiments aiming for larger differences would be extremely helpful for continued study of the q-profile impact on transport.

Acknowledgments

This work, supported by the European Communities under the contract of Association between EURATOM/FOM and EURATOM/CEA, was carried out within the framework of the European Fusion Programme with financial support from NWO. The views and opinions expressed herein do not necessarily reflect those of the European Commission. This work is supported by NWO-RFBR Centre-of-Excellence on Fusion Physics and Technology (Grant nr. 047.018.002). The authors are grateful to W Goedheer, G Sips, I Voitsekhovitch and E Westerhof for fruitful discussions.

© Euratom 2012.

References

[1] Gormezano C *et al* 2007 Progress in the ITER Physics Basis Chapter 6: Steady state operation 2007 *Nucl. Fusion* **47** S285
[2] Luce T C *et al* 2003 *Nucl. Fusion* **43** 321
[3] Sips A C C *et al* 2002 *Plasma Phys. Control. Fusion* **44** B69
[4] Joffrin E *et al* 2005 *Nucl. Fusion* **45** 626
[5] Isayama A *et al* 2003 *Nucl. Fusion* **43** 1272
[6] Menard J E *et al* 2007 *Nucl. Fusion* **47** S645
[7] ITER Physics Expert Group on Confinement *et al* 1999 ITER Physics Basis Chapter 2: Plasma confinement and transport *Nucl. Fusion* **39** 2175
[8] Wade M R *et al* 2005 *Nucl. Fusion* **45** 407
[9] Sips A C C *et al* 2007 *Nucl. Fusion* **47** 1485
[10] Joffrin E *et al* 2010 *Proc. 23rd Int. Conf. on Fusion Energy 2010 (Daejeon, South Korea 2010)* (Vienna: IAEA)
[11] Petty C C *et al* 2004 *Phys. Plasmas* **11** 2514
[12] McDonald D C *et al* 2004 *Plasma Phys. Control. Fusion* **46** A215
[13] Maggi C F *et al* 2007 *Nucl. Fusion* **47** 535
[14] Maggi C F *et al* 2010 *Nucl. Fusion* **50** 025023
[15] McDonald D C *et al* 2008 *Plasma Phys. Control. Fusion* **50** 124013
[16] Politzer P A *et al* 2008 *Nucl. Fusion* **48** 075001
[17] Mantica P *et al* 2011 *Phys. Rev. Lett.* **107** 135004
[18] Mantica P *et al* 2011 *Plasma Phys. Control. Fusion* **53** 124033
[19] Waltz R E *et al* 1997 *Phys. Plasmas* **7** 2482
[20] Guo S C and Romanelli F 1993 *Phys. Fluids* B **5** 520
[21] Bourdelle C *et al* 2002 *Nucl. Fusion* **42** 892–902
[22] Fourment C *et al* 2003 *Plasma Phys. Control. Fusion* **45** 233
[23] Hoang G T *et al* 2003 *Phys. Plasmas* **10** 405
[24] Hoang G T *et al* 2001 *Phys. Rev. Lett.* **87** 125001
[25] Artaud J F *et al* 2010 *Nucl. Fusion* **50** 043001
[26] Kinsey J E *et al* 2005 *Phys. Plasmas* **12** 052503
[27] Petty C C *et al* 2004 *Phys. Plasmas* **11** 3
[28] Bourdelle C *et al* 2007 *Phys. Plasmas* **14** 112501
[29] Citrin J *et al* 2010 *Nucl. Fusion* **50** 115007
[30] Hobirk J *et al Plasma Phys. Control. Fusion.* submitted
[31] Stober J *et al* 2007 *Nucl. Fusion* **47** 728
[32] Gunter S *et al* 1999 *Nucl. Fusion* **39** 1535
[33] Casper T A *et al* 2007 *Nucl. Fusion* **47** 825
[34] Petty C C *et al* 2009 *Phys. Rev. Lett.* **102** 045005
[35] Menard J E *et al* 2006 *Phys. Rev. Lett.* **97** 095002
[36] Na Yong-Su *et al* 2006 *Nucl. Fusion* **46** 232
[37] Fischer R *et al* 2010 *Fusion Sci. Technol.* **58** 675–84
[38] Schneider M *et al* 2009 *Nucl. Fusion* **49** 125005
[39] Schneider M *et al* 2011 *Nucl Fusion* **51** 063019
[40] Eriksson L-G *et al* 1993 *Nucl. Fusion* **33** 1037
[41] Huysmans G T A *et al* 1991 *CP90 Conf. on Computational Physics (Amsterdam)* (Singapore: Word Scientific) p 371
[42] Houlberg W A *et al* 1997 *Phys. Plasmas* **4** 3230
[43] Cenacchih G *et al* 1988 ENEA RT/TIB/88/5
[44] Voitsekhovitch I *et al* 2009 *Nucl. Fusion* **49** 055026
[45] Joffrin E *et al* 2010 *EPS Conf. on Plasma Phys. (Dublin, Ireland)* P1.1047, http://ocs.ciemat.es/EPS2010PAP/pdf/P1.1047.pdf
[46] Kinsey J E *et al* 2005 *Nucl. Fusion* **45** 450
[47] Imbeaux F *et al* 2005 *Plasma Phys. Control. Fusion* **47** B179
[48] Kinsey J E *et al* 2008 *Phys. Plasmas* **15** 055908
[49] Kinsey J E *et al* 2010 *Phys. Plasmas* **17** 122315
[50] Kinsey J E *et al* 2005 *Phys. Plasmas* **12** 062302
[51] Highcock E G *et al* 2010 *Phys. Rev. Lett.* **105** 215003
[52] Barnes M *et al* 2010 *Phys. Rev. Lett.* **106** 175004
[53] Versloot T W *et al* 2011 *Nucl. Fusion* **51** 103033
[54] Weiland J *et al* 1989 *Nucl. Fusion* **29** 1810
[55] Solomon W M *et al* 2006 *Phys. Plasmas* **13** 056116
[56] Crombé K *et al* 2005 *Phys. Rev. Lett.* **95** 155003
[57] Field A R *et al* 2009 *Plasma Phys. Control. Fusion* **51** 105002
[58] Jenko F *et al* 2001 *Phys. Plasmas* **8** 4096